南北磁気共役点での高速撮像による
オーロラ爆発と脈動オーロラの研究

Study of
auroral breakup and pulsating aurora by high-speed imaging
at north–south magnetic conjugate stations

Herbert Akihito Uchida

FOR THE DEGREE OF DOCTOR OF PHILOSOPHY

October 2020

Department of Polar Science

School of Multidisciplinary Sciences

The Graduate University for Advanced Studies, SOKENDAI

Contents

Acknowledgments

There are many people I would like to thank for their help in conducting this research. First of all, I would like to express my sincere gratitude to my supervisor, Dr. Ryuho Kataoka, for generously giving me scientific advices from a wide range of perspectives and many opportunities including observation activities at various places over the world. Discussions with him have always given me the energy to drive my research, and he showed me how to enjoy science. I would also like to gratefully thank my supervisor, Dr. Koji Nishimura, who provided me many important technical advices on the development of the new high-speed imager system. His sincere advice about my future directions allowed me to proceed my research activities in a positive mind.

My sincere thanks go to the help of my colleagues of the 59th Japan Antarctic Research Expedition, who spent the whole 14 months together in the Antarctic. This research was only realized owing to their cooperation. I am honored to be able to participate in the expedition team, and I am grateful to the National Institute of Polar Research for giving me this opportunity.

The camera installation and observation at Tjörnes, Iceland was supervised by Prof. Akira Kadokura. Together with my colleague Kiyoka Murase, who also helped a part of my research, we learned a lot on the field works as well as the scientific advises. Kogure-kun, Fujiwara-san, Shigeyama-kun, and Septi, who shared the laboratory room at the institute with me, kindly shared a patience to be a PhD student at SOKENDAI. Finally, I would also like to thank all of the member of our laboratory group, Space and Upper Atmospheric Sciences Group, especially for their daily support from Takahama-san, Shiraishi-san.

Abstract

An understanding of the auroral substorm phenomenon is one of the most important requirements in the research of magnetospheric and ionospheric plasma dynamics. This thesis is dedicated to observationally constraining the mechanism of the energy release in the ionosphere associated with the substorms by using a new ground-based high-speed imaging system developed by the author. As a unique point, the author selected a frame rate of 100 frames per second, which is sufficiently high for capturing new auroral phenomena beyond the human eye, and a classical video rate of ~30 fps. Optical filters and systems were omitted, and standard C-mount lenses were attached directly to an electron-multiplying charge-coupled device (EMCCD) camera to facilitate changing the lens from fish-eye to telescopic to alter the field-of-view. This newly developed imaging system was installed by the author at the northern and southern magnetic conjugate stations at Tjörnes Station, in Iceland (magnetic latitude of 66.27°) and Syowa Station in Antarctica (magnetic latitude of −66.33°). The author attended the Japanese Antarctic Research Expedition overwinter program to realize both all-sky and narrow field-of-view high-speed imaging at Syowa Station. During this period, more than 200 TB of images were recorded on hard disk drives. The most notable scientific results were then obtained from a successful observation campaign among those conjugate ground-based stations and the Arase satellite on September 22, 2018. A detailed analysis of these results provides the scientific basis of this thesis.

The first finding pertains to the asymmetric development of the poleward expansion at the auroral breakup as identified at the north–south conjugate points. The initial brightening auroras were longitudinally shifted for 1.7–2.3 magnetic local time (MLT)

from the nominal conjugate points, which is consistent with the empirical relationship dependent to the y-component of the interplanetary magnetic field. Interestingly, the subsequently observed propagating auroras were directed in opposite directions at the northern and southern conjugate points, i.e., eastward (westward) propagation was noted in the Northern (Southern) Hemisphere. Because the propagation directions correspond to the direction of the asymmetric ionospheric equivalent currents at the northern and southern conjugate points, it is suggested that the ambient ionospheric Hall current plays an essential role in the asymmetric development, as theoretically expected based on global simulations by Ebihara and Tanaka (2015b; 2018). The result explained above was published in Geophysical Research Letters (Uchida et al., 2020).

High-speed imaging enables in-depth examination of the expected shear motion of auroras, which should appear at the leading edge of propagating auroras. The identified shear motions are in the opposite direction to those expected from the simulation works of Ebihara and Tanaka in both hemispheres. This discrepancy might contribute to improving future global simulations. It is also needed to observationally examine that similar shear motions can be identified in many other events of poleward expansion in our data set of high-speed imaging.

The second finding was made during the early recovery phase of the same substorm event by using ground-based high-speed imaging and the in-situ burst-mode observation of plasma waves by the Arase satellite. In contrary to standard knowledge of pulsating auroras containing an intensity variation of a few or several seconds with 3±1 Hz modulation, a rapid pulsating aurora at ~20 Hz was identified by our narrow FOV imager at Syowa Station that was not detected by our all-sky imager. The Arase satellite simultaneously observed ~20 Hz intensity variations of whistler mode waves, providing

the first evidence that whistler mode waves can cause the pulsating auroras in the fastest regime far beyond the well-known 3 Hz modulation.

This thesis therefore successfully demonstrates that the high-speed imaging observation of auroras beyond the human eye is essential to newly identify and understand fine-scale auroral dynamics and to visualize the wave-particle interactions occurring in the magnetosphere. In future work, a maintenance-free observation system needs to be developed to continue the high-speed observations. In addition, development of a new browsing system is needed to quickly review huge amounts of data to find interesting events other than the substorm event occurring on September 22, 2018. This thesis provides several basic ideas for such developments based on the experience obtained throughout our research activities.

1. Introduction

1.1. Auroral substorm

Auroras appear in various dynamic forms. The most outstanding form is the auroral breakup, in which part of the auroral oval suddenly brightens and expands poleward for a few tens of minutes. The global disturbance in the magnetosphere–ionosphere coupled system associated with the auroral breakup is known as a substorm according to the global auroral morphology identified in the pioneering work of Akasofu (1964). **Figure 1-1** summarizes the cyclic development of auroral substorms, as depicted from the careful examination of the ground-based all-sky images obtained from world-wide observatories. Since the discovery of auroral substorms, numerous satellite observations in the space age followed by cutting-edge simulation research have played important roles in identifying and clarifying the key aspects, respectively. However, the complete mechanisms of substorms have remained unknown for more than a half century. This doctoral thesis is also dedicated to reveal a part of the substorm, especially focusing on the active role of the ionosphere in the explosive energy consumption. The following paragraphs briefly introduce the current understanding of the basic sequence of a substorm phenomenon, as partly modified from Akasofu's original study based on recent simulation research of Ebihara and Tanaka (2015a; 2015b; 2018).

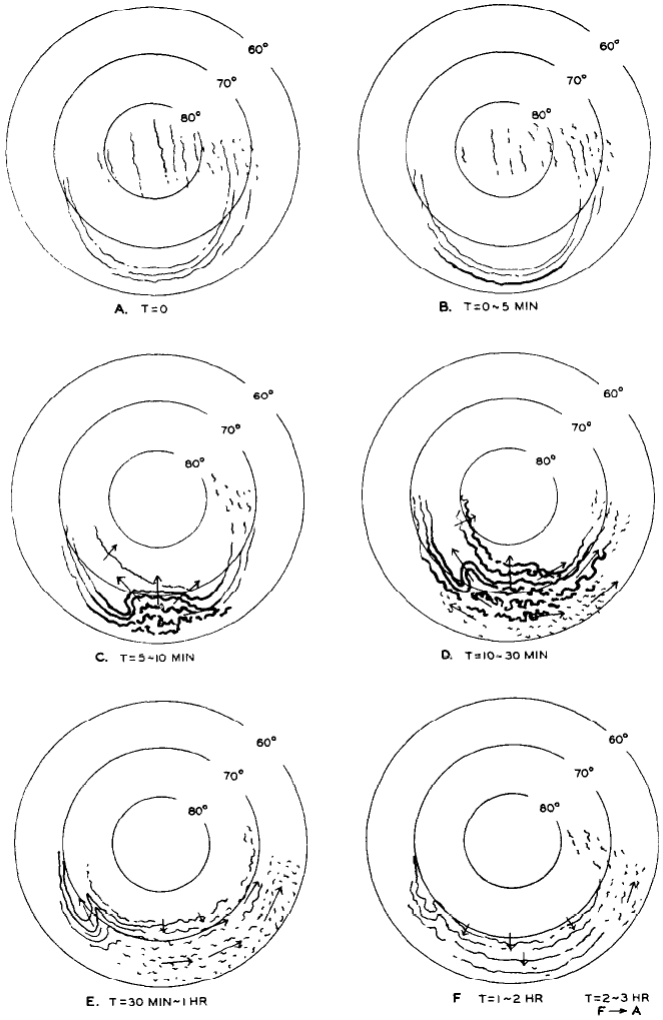

Figure 1-1: Schematic diagram of the global development of an auroral substorm. The center of the concentric circles in each stage is the north geomagnetic pole, and the Sun is toward the top (after Akasofu (1964)).

(1) The growth phase begins prior to that shown in **Figure 1-1A**. During the growth phase, east–west aligned arcs move equatorward driven by solar wind as explained below. The interplanetary magnetic field (IMF) is embedded in the solar wind. The southward directed IMF can interact with the magnetosphere to accumulate the electromagnetic energy and to drive large-scale plasma convection in the magnetosphere. This convection

stretches the magnetic field in the night side and results in an increase in the size of the entire auroral oval. The equatorward movement of the quiet arcs are consistent with the thinning tail and expanding oval. The evolution of the structured auroras during the growth phase has been detailed by Kadokura et al. (2002).

(2) Part of the auroral oval suddenly brightens in the phase known as initial brightening (**Figure 1-1B**), which is recognized as the onset of the auroral breakup. The trigger of this sudden brightening is associated with the beginning of the reconnection in the thin current sheet, or global reconstruction of the magnetic field topology of the magnetosphere, which can release part of the accumulated energy toward the ionosphere. During the last half century, a numerous study have been conducted to elucidate the triggering mechanism of substorms, including recent simulation research by Tanaka et al. (2019b).

(3) The bright spot expands poleward (**Figure 1-1C**) to form an area known as the bulge. This step, known as the expansion phase, causing significant energy consumption in the ionosphere. The westward expansion of the bulge is known as the westward traveling surge, which has a typical traveling speed of a few kilometers per second (Akasofu, 1964). As shown in **Figure 1-2**, the fine structure of the bulge includes a north–south (N–S) aurora as well as an eastward-propagating aurora (Nakamura et al., 1993). The evolution of N–S aurora and the associated current system have been investigated in detail by unmanned observatories in Antarctica (Kadokura et al., 2008).

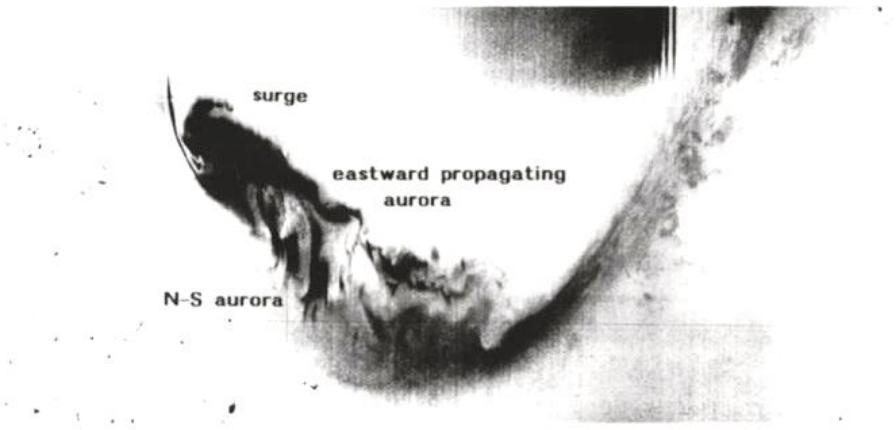

Figure 1-2: Example of a structured bulge including the surge, N–S aurora, and eastward-propagating aurora, as observed by the DMSP F6 satellite (after Nakamura et al. (1993)).

1.2. Auroral breakup

The details of auroral structures appearing in the expansion phase is one of the main targets of this thesis. It is noteworthy that in addition to the westward traveling surge, eastward-propagating auroral structures have been observed after the initial brightening by Nakamura et al. (1993), as also depicted in **Figure 1-2**. Carbary et al. (2000) showed that ~35% of the centroid of the expanding aurora bulge moved eastward using the data of the Ultraviolet Imager onboard the Polar satellite during January 1997. Liou et al. (2002) showed an example that the eastern edge of a bulge expands at 4.0 km s^{-1}, which exceeds the typical traveling speed of a westward traveling surge, at 0.1 to 2.4 km s^{-1} (Liou et al., 2002). As shown in **Figure 1-3**, Liou et al. (2006) also reported that eastward-moving auroral bulges are as common as westward-moving ones during the substorm expansion phase. Liou and Ruohoniemi (2006) explained westward and eastward expansions with global plasma convection.

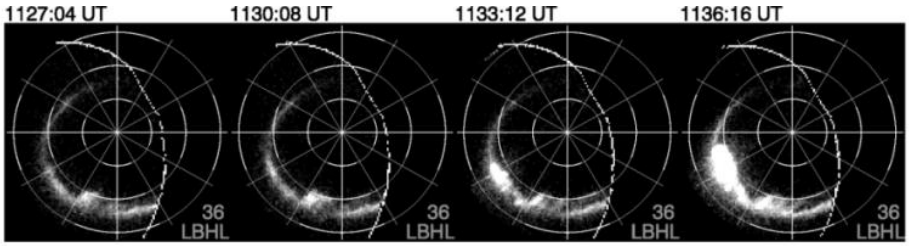

Figure 1-3: Example of the global development of a westward traveling surge as observed by the Polar UVI (after Liou et al. (2006)). The onset occurred at ~1130 UT on March 7, 1997. The auroral images are mapped onto the magnetic latitude–magnetic local time (MLT) coordinate. The magnetic latitudes are indicated every 10°, and the MLT is indicated every 2 h. The top of the image indicates local noon, and dawn is indicated at the right. The time stamp indicates the center of each snapshot accumulated in 36.8 s. The white dotted line in each panel indicates the FOV of the UVI.

Theoretical models have been proposed to explain the evolution of westward traveling surges owing to polarization charges in the ionosphere (e.g., Rothwell et al., 1984; Kan and Kamide, 1985). Recently, Ebihara and Tanaka (2015b; 2018) used a global magnetohydrodynamic (MHD) simulation of the magnetosphere coupled with the ionosphere to develop a generalized model of a westward traveling surge. In particular, when the gradient of the Hall conductivity is a nonzero value, the surge can travel in the direction of the Hall current owing to the positive charge accumulated at the leading edge of the surge, which increases the upward field-aligned current (FAC). Based on the analysis of their simulation results, Ebihara and Tanaka (2015b; 2018) suggested a fundamental mechanism such that the surge should develop in the direction of the ionospheric Hall current. The surge can therefore develop eastward if the background Hall current is directed eastward.

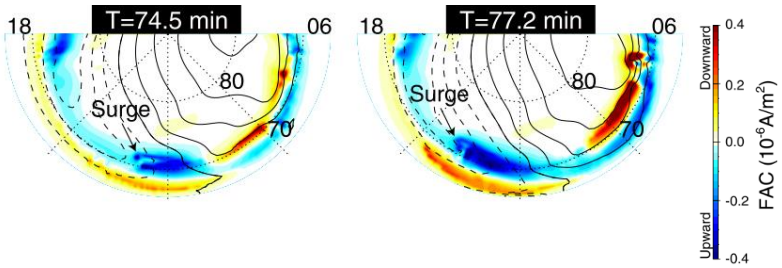

Figure 1-4: Simulation results of a westward traveling surge as reported by Ebihara and Tanaka (2018). The initial brightening occurred at T = 69.4 min. The field-aligned current (FAC) in the ionosphere is color coded; blue and red colors indicate upward and downward FACs, respectively. The contour lines represent the ionospheric electric potential at intervals of 5 kV. The solid and dashed lines indicate the positive and negative potentials, respectively.

Here, Hall and Pedersen currents are ionospheric horizontal currents that flow in the direction of $-\mathbf{E}\times\mathbf{B}$ and $\mathbf{E}$, respectively. Roughly speaking, the Hall current dominates in the E region, whereas the Pederson current dominates in the F region. Fukushima's theory (Fukushima, 1976) uses height-integrated conductivities to relate the horizontal magnetic field deviation at the ground to the Hall current in the ionosphere, which leads to the basic concept of the equivalent current.

It is also important to note here that the divergence of the height-integrated Hall current becomes zero if all of the conductivities are uniform in horizontal directions. However, in more realistic situations of inhomogeneous conductivity, the Hall current diverges to connect with the field-aligned current (FAC). This current closure via the Hall current becomes important when the horizontal gradient of the conductivity is strong.

Further, when it occurs, the vorticity of $\mathbf{E} \times \mathbf{B}$ drifting plasma can become opposite of that in a uniform conductivity case. This is a basic principle as illustrated in **Figure 1-4**.

1.3. Pulsating aurora

After the expansion phase, the substorm enters the recovery phase, in which diffuse and patchy auroras are dominant. The most outstanding type of a diffuse aurora is a pulsating aurora, in which the luminosity changes quasi-periodically. The main pulsation cycle is several to several tens of seconds long, with the transition resembling an on–off switch (Yamamoto, 1988). Intensity modulation of the luminosity within the "on" time of a pulsation is sometimes found, with a frequency of 3±1 Hz (Royrvik and Davis, 1977). Rocket observations have identified electron flux modulations for both the main pulsation and so called 3±1 Hz modulation (Sandahl et al., 1980).

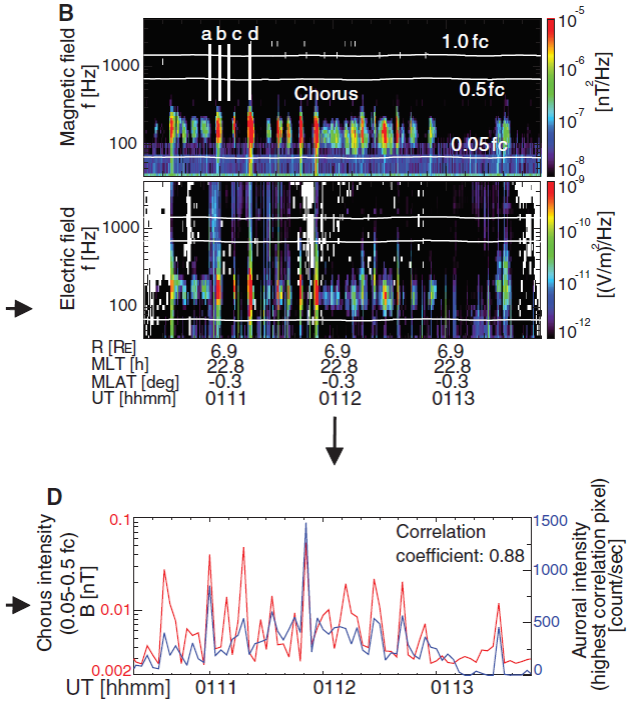

Figure 1-5: Pulsating aurora observed by the ground-based all-sky imager and plasma waves observed by the THEMIS-A spacecraft on February 15, 2009 (after Nishimura et al., 2010). (B) Lower-band chorus waves observed by THEMIS-A. The horizontal white

lines are 0.05, 0.5, and 1.0 fc. (D) Correlation between the integrated lower-band chorus (red) and the auroral intensity (blue).

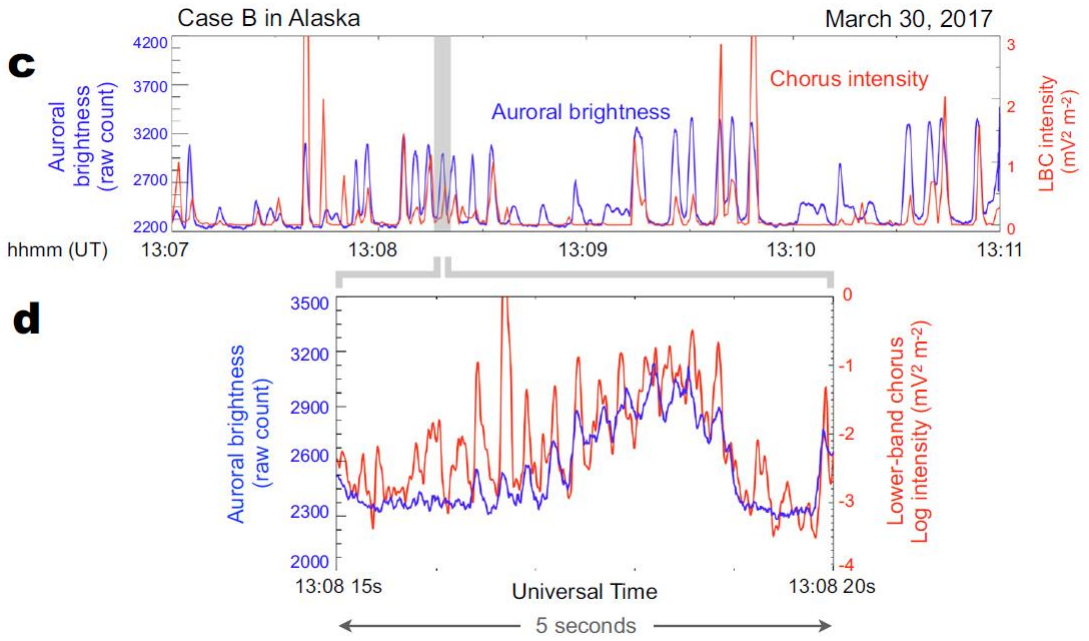

Figure 1-6: Example of good correlation found between the time-series of pulsating aurora luminosity and chorus intensity (after Hosokawa et al., 2020). The blue line represents the auroral luminosity, whereas the red line shows the wave power integrated over the lower band chorus.

Recent satellite and ground-based conjugate observations have shown that chorus waves are responsible for the main pulsation (Nishimura et al., 2010), as illustrated in **Figure 1-5**. The one-to-one correlation of chorus wave elements and the ~3 Hz internal modulation of auroral luminosity has also been proved (Hosokawa et al., 2020), as shown in **Figure 1-6**. The fundamental cause of pulsating auroras must therefore be energetic electrons that repeatedly precipitate into the atmosphere via wave–particle interaction

(e.g., Nishimura et al., 2010; Kasahara et al., 2018; Ozaki et al., 2018; Hosokawa et al., 2020). The remaining problem includes the fastest temporal variation in the pulsating aurora in the frequency range beyond the ultra low frequency range, as identified by Kataoka et al. (2012) and shown in **Figure 1-7**.

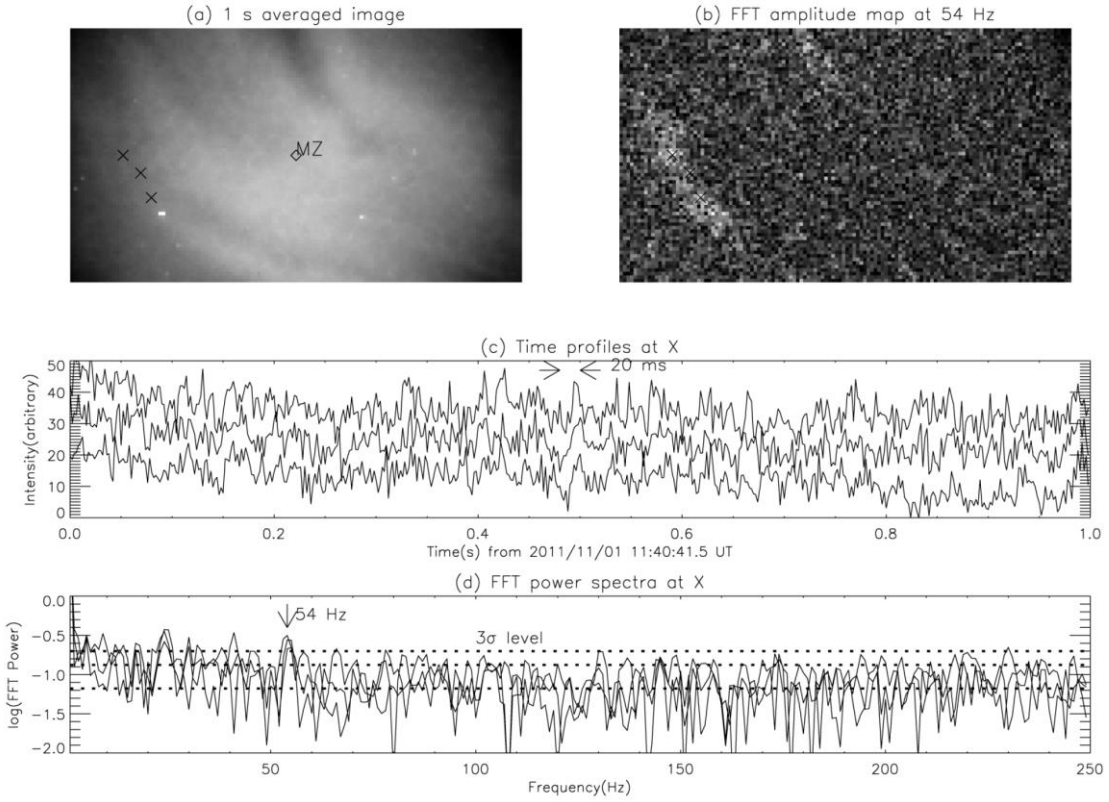

Figure 1-7: (a) 1 s averaged image of aurora. The magnetic zenith is indicated as MZ. (b) Distribution map of FFT amplitude at 54 Hz. (c) Time profiles of aurora emission intensity at three different points X in the aurora image, where high-speed modulation of 54 Hz was confirmed by FFT spectrum analysis. (d) FFT power spectra of panel (c). The white noise levels of one, two, and three times the standard deviation are shown by the dotted lines.

1.4. Purpose of this thesis

Since the 1980s, the above-mentioned picture of auroral substorms and subsequent auroral structures have been clarified by satellite global images (Craven and Frank, 1985; Carbary, 2000; Liou et al., 2006). However, ground-based observations have also played an essential role in clarifying these auroral substorm phenomena. For example, Ieda et al. (2018) reported differences of a several minutes between the onset times of auroral breakup events, as determined from ground-based all-sky imagers and global images captured from the spacecraft. The detailed structures occurring at the beginning of an auroral breakup can therefore be captured only by ground-based imaging observations. Although ground-based all-sky cameras are affected by the limited field-of-view (FOV) and weather conditions, their high temporal and spatial resolutions are essential for identifying the fine dynamic structures. In this thesis, a cutting-edge camera system is newly developed to study the auroral substorm in great detail. The hypothesis of asymmetric traveling surges associated with the ionospheric Hall current can be evaluated by ground-based observations of the surge structure in both the Northern and Southern Hemispheres.

It should be noted that the conjugate aurora itself is not a new area of study. The auroras in the conjugate region are sometimes strongly correlated, such as during the time of simultaneous breakup (DeWitt, 1962), whereas the subsequent development of the breakup aurora can be asymmetric (e.g., Sato and Saemundsson, 1987). The latitudinal displacement of breakup auroras has also been observed (Wescott, 1966; Stenbaek-Nielsen et al., 1972; Motoba et al., 2010).

The cause of the fastest modulation of pulsating auroras also remains unsolved mainly because of the technological limitations of the observation systems. Owing to the recent development of sensitive cameras, the mechanisms leading to the fastest variation can also be investigated in greater detail. The cause of the fastest variation in auroras, e.g., plasma waves that can resonate and scatter energetic electrons, can also be resolved by conjugate in-situ observations of energetic particles and plasma waves. The in-situ observation data from the Arase satellite have been available since March 2017, and the campaign observation has been conducted with ground-based observations.

The purpose of this thesis is to observationally constrain the physical mechanism connecting the magnetosphere and the ionosphere by analyzing the poleward expansion and pulsating aurora based on ground-based high-speed observation. We installed identical all-sky high-speed cameras at magnetically conjugate observatories in the Northern and Southern Hemisphere because the conjugate and high-speed observations can provide unique clues to identify the possible mechanisms of auroral substorms. For that purpose, we needed to develop an observation system for realizing the high temporal resolutions and timing accuracy. The instrumentation and the development of the high-speed imager system are described in Chapter 2. In Chapter 3, an overview of the event of interest and the obtained data are explained. In Chapter 4, asymmetric surge development is shown and discussed in detail. In Chapter 5, rapid pulsation is shown and discussed. In Chapter 6, the entire event is discussed and summarized, and the future research directions are explained. Finally, Chapter 7 summarizes the concluding remarks.

2. Development of high-speed aurora imager

The author has been deeply involved in the development, installation, maintenance, and running of the high-speed aurora imagers (HAIs) used in this study. A new triggering circuit board known as the Uchida Triggering Controller (UTC-board) was developed and installed in the observation systems at multiple observatories to make highly accurate time-based observations in remote areas. The background of the system development is described in **Section 2.1**, and the design and specifications of the new triggering system are described in **Section 2.2**. The synchronization technique between the cameras and a personal computer (PC) as well as the sequences of the image acquisition behavior are explained in **Section 2.3**. The accuracy of the absolute time-detailed sequence of the image acquisition behavior is described in **Section 2.4**.

2.1. Background

The time resolution of the imaging observation of auroras has become much higher in recent years with the development of imaging devices. To capture the appearances of high temporal and spatial variation in auroras, several high-speed imaging systems have been developed. For example, the Auroral Structure and Kinetics (ASK) instrument is a multi-monochromatic ground-based optical imager consisting of an Electron Multiplying Charge Coupled Device (EMCCD) detector with a narrow FOV lens pointing toward magnetic zenith. This instrument provides simultaneous images of auroras in three different spectral bands at a resolution of 5 frames per second (fps) (Dahlgren et al., 2008). By calculating the precipitation energy from the observed spectra, they successfully revealed the relationship between fine-scale auroras and the precipitating energy and flux.

The ASK instrument has a horizontal spatial resolution of 20 m at an altitude of 100 km. They found a thinnest structure of ~200 m in width. Haerendel (1999) reported the narrowest filament of 100 m width, which appeared only when the exposure was as short as 2.5 ms. He discussed the importance of higher frame rate because the fine spatial structure and the fast temporal variation in auroras can become smeared out in the image during the exposure.

When observing the rapidly varying auroras, prompt emissions are the focus, particularly the blue emission of N_2 and the near-infrared emission of N_2^+. At that time, the bright and slow emissions come to discussion. The dominant green line at 557.7 nm and the red line at 630.0 nm are the emission from the forbidden transitions of atomic oxygen, which have transition times of 0.74 s and 110 s, respectively. This long-lived, high-intensity luminescence is thought to remain like afterglow and smear out the temporal and spatial variations of the aurora. This led to the need for optical filters in observation. Samara et al. (2012) investigated the effectiveness of the BG3 glass filter, which cuts off the 557.7 nm and 630.0 nm emissions yet passes the prompt emissions. They found that although the BG3 glass filter reduces the overall signal levels and increases the relative intensity variations of the fast pulsating aurora by 0.5%–2.1%, slight decreases of the signal-to-noise ratio also occur. This means that optical glass filters do not enhance the ability to quantify the rapidly varying auroral structures. Therefore, the HAI system was designed to observe all wavelengths without using a glass filter.

Ground-based HAIs have been used for aurora observation since 2010 (Yaegashi et al., 2011). Scientific Complementary Metal Oxide Semiconductor (sCMOS) cameras are excellent tools in terms of the readout speed, whereas EMCCD cameras have better optical sensitivity over the readout speeds. Both of these features are important for

capturing the true shapes of the aurora, which consist of thin structures, rapid movement, fast beats in luminosity, and sometimes weak glow in brightness. For this reason, both of these camera types are used at multiple stations. Since 2014, HAI observation systems have been installed at observatories as unmanned automated systems. Various techniques have been introduced to retrieve data of the highest quality, which has caused differences in the evolution of the observation system configuration every year at multiple stations. Especially, timestamping of the acquired data is a key problem in high-speed imaging.

The first HAIs were installed at Poker Flat Research Range (PFRR, 65.12°N, 212.57°E, and magnetic latitude 65.81°) in February 2014 and were operated until April 2014 (Kataoka et al., 2015; Fukuda et al., 2016). Two sCMOS cameras (Orca-Flash4.0 V2, Hamamatsu) installed at the site were equipped with the same narrow FOV lens, at 50 mm/F 1.2. One camera was mounted with an RG665 glass filter to eliminate the green and red auroral emission lines at 557.7 nm and 630.0 nm, respectively, with long emission time constants and was operated with a time cadence of 200 fps. The other had no filter mounted and was operated with a time cadence of 50 fps. At that time, the image acquisition was triggered by the “internal trigger” of the camera, and the timestamp of each image was the time at which the PC communicated with the camera. To obtain more accurate timestamps, a timing system was introduced by adding a light-emitting diode (LED) at the edge of the FOV that emits in synchronization with the pulse-per-second (PPS) signal from a Global Positioning System (GPS) receiver. This method marked the start frame of every second, and the absolute time of each frame was obtained under the assumption that the error of the PC time was within ±0.5 s. The flash of the LED light covered approximately two-thirds of the FOV and was treated as a contaminant. A digital single lens reflex (DSLR) camera (D4, Nikon) with a fisheye lens (8 mm/F 2.8, NIKKOR)

was also installed alongside the sCMOS cameras and captured color images every 10 s.

From November 2014 to April 2015 at PFRR, the timing LEDs were removed; the triggering modes of the cameras were set to “Start Trigger Mode”; and a signal from the GPS receiver was used to trigger the beginning of acquisition at 0 s every minute. A circuit board was designed by Koji Nishimura (NIPR) for this purpose. Although the GPS receiver module outputs the PPS signal only when a GPS satellite is visible, it begins its own clock inside the module and outputs a minute signal at 0 s every minute. The designed circuit board logically sums the PPS signals and the minute signals to create a stable trigger signal even when no GPS satellites were visible. This method guaranteed the absolute time of the first acquired image so that the absolute time of each frame was calculated by the time elapsed from the first frame. However, sometimes the number of visible GPS satellites was insufficient for the receiver to emit PPS signal at high latitudes such as that at PFRR. In this case, the absolute time accuracy of the trigger signal depends on the internal clock of the GPS module, which increases the error of the absolute time of the trigger signal. It was also preferred to append timestamps for every acquisition frame to facilitate the analysis easier that could contain dropped frames.

Because a PC controls the cameras and handles the acquired image data, the timestamps also depends on the PC time. Although the PC time was corrected by the Network Time Protocol (NTP) server through the internet every minute, it included an absolute time error of several tens of milliseconds and instability in the time cadence. The time cadence of the image acquisition increased with more than 100 fps (Fukuda et al., 2017); therefore, the stability of the acquisition frame rate had to be improved to conduct cutting-edge ground-based high-speed imaging. Further, a pair of HAIs has been deployed at geomagnetic conjugate stations (Tjörnes (TJO) in Iceland and Syowa station

(SYO) in the Antarctic region) to study the conjugate aurora phenomena, which requires high accuracy of the absolute time stamp on each image to ensure the simultaneity. Furthermore, the HAI observation aimed to capture the fast fluctuations of auroras in conjugate with the ARASE satellite, which requires high time-stamp accuracy for detailed time-based data analysis.

In this study, the UTC-board was developed and installed in a pair of all-sky HAIs with identical configurations at TJO and SYO. Additionally, another HAI with a UTC-board equipped with a narrow FOV lens was installed and operated at SYO to capture the auroral fine structures and fast variations. The all-sky imager at TJO and the all-sky and narrow FOV imagers at SYO are shown in **Figure 2-1** and **Figure 2-2**. Each system consists of an EMCCD camera (ImagEM X2 C9100-23B, Hamamatsu Photonics), as shown in **Figure 2-3**. The all-sky imager was equipped with a fish-eye lens (Fujinon FE185C086HA-1), and the narrow FOV imager was equipped with a telephoto lens (NIKKOR 105mm f/1.4). None of the imagers used optical filters. The EMCCD has an original pixel array size of 512 × 512. To reduce the data storage and to enhance the sampling rate at 100 fps, 2 × 2 binning was applied. As a result, each saved image had a pixel array size of 256 × 256.

From 2017 to 2019, HAIs equipped with the newly developed UTC-board have played important roles in the ground-based support observation of the Arase (Exploration of Energization and Radiation in Geospace, ERG) satellite project.

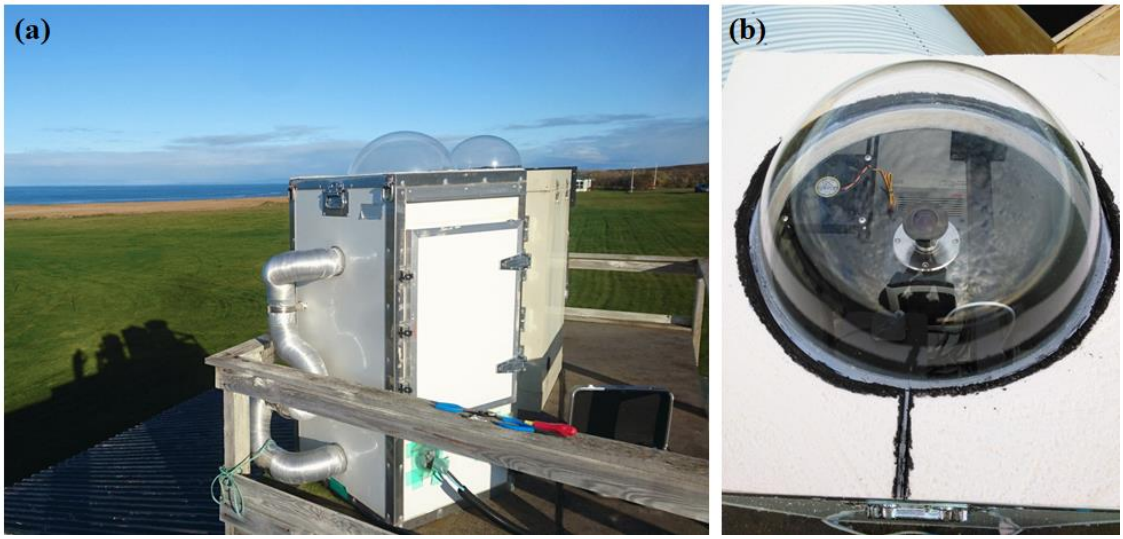

Figure 2-1: Overall view of the all-sky imager installed at TJO. (a) View from west to east; (b) image facing the acrylic dome.

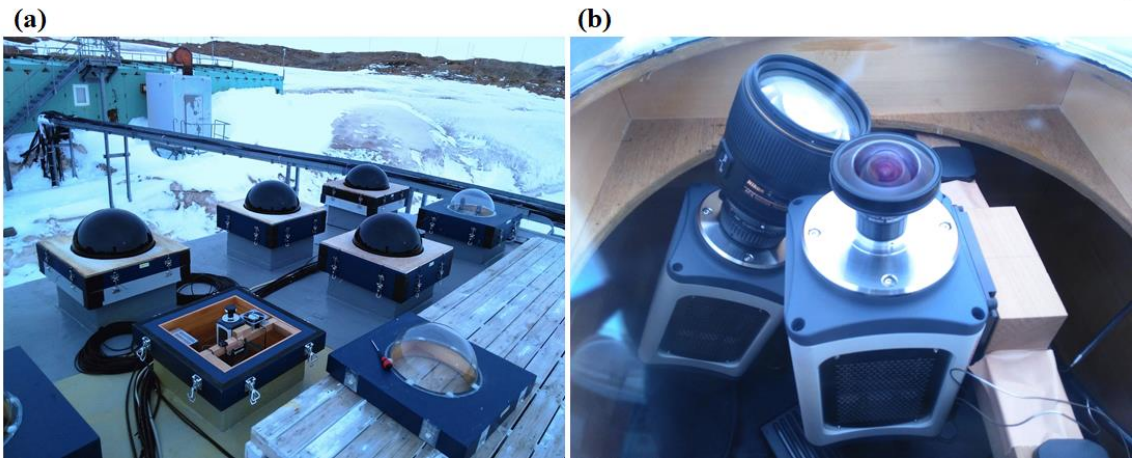

Figure 2-2: Overall view of the all-sky imager and the narrow FOV imager installed at SYO. (a) The dome was open while the all-sky imager was being installed. (b) Image facing the acrylic dome after the installation of both the all-sky imager and the narrow FOV imager.

Figure 2-3: EMCCD camera (ImagEM X2 C9100-23B, Hamamatsu Photonics)

2.2. Component design

A schematic diagram of the component design is shown in **Figure 2-4**. In the previous design (**Figure 2-4a**), the trigger pulses were generated inside the camera based on its internal clock. Here, the timestamps are determined on the basis of the PC time once the image data arrives at the PC. The basic concept of the UTC-board is to generate the trigger pulses and timestamps at the same time within the UTC-board (**Figure 2-4b**). The trigger pulses are given to the camera, and the timestamp data are sent to the PC. In this manner, the uncertainty in the PC time can be neglected, and the timestamps can be completely matched with each trigger pulse. Once the camera receives one trigger pulse and captures an image, it sends the image data to the PC, and the observation software installed in the PC combines the image data and the timestamp data.

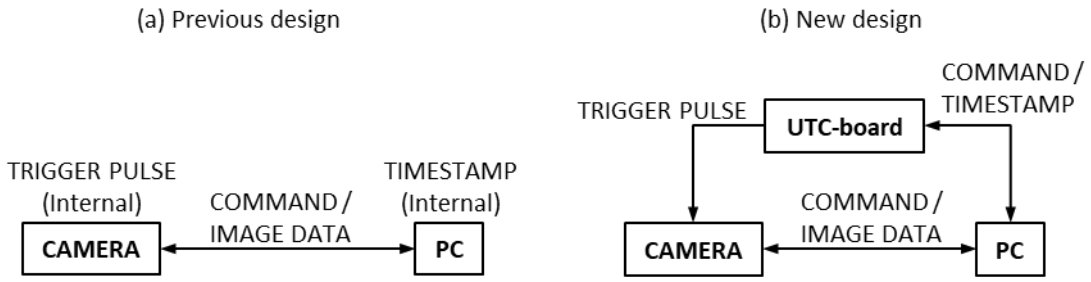

Figure 2-4: Comparison of the (a) previous and (b) new schematic diagrams of the HAI system. In (b), the trigger pulse and timestamp are generated at the same time within the UTC-board.

A component diagram of the UTC-board is shown in **Figure 2-5**. The board consists of four main components (shown in blue), three indicator LEDs (shown in red), and five interfaces that connect the board with the other equipment. The selection of devices used for each of the components, indicators, and interfaces is explained.

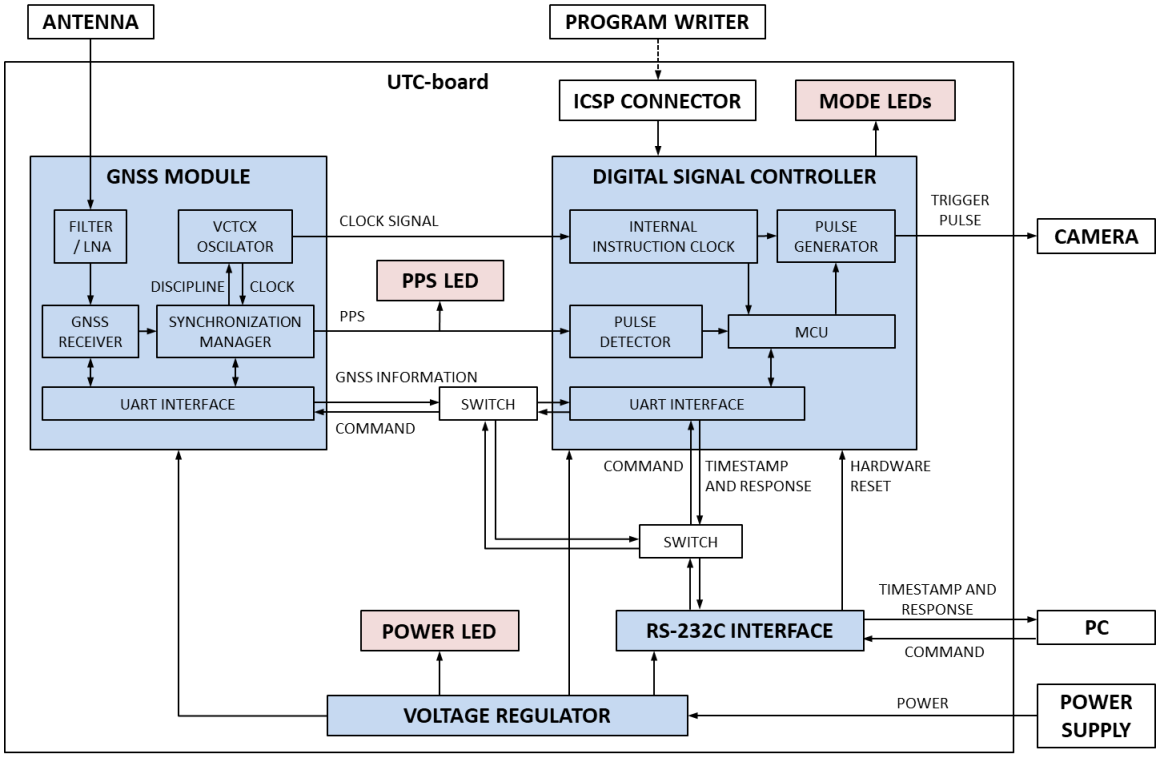

Figure 2-5: The component diagram of the UTC-board and the connection with other devices that comprise the HAI observation system.

2.2.1. Main components

In this section, the four main components that comprise the UTC-board are explained.

(1) DIGITAL SIGNAL CONTROLLER

A digital signal controller (DSC) is a programmable microcomputer package that contains a central processing unit (CPU), non-volatile memory, and several peripheral functionalities such as a serial communication unit or a timer unit. Therefore, it is applicable for processing signals and for controlling the other modules. The dsPIC33FJ64GP802 (Microchip Technology) unit was selected as the DSC. The

firmware is written in C-language, compiled by the MPLAB XC C Compiler, and written in to the DSC by the PICkit 3 writing device. The DSC is operated by an oscillator synchronized with the Global Navigation Satellite System (GNSS) time output by the GNSS module. The DSC communicates with the GNSS module through the Universal Asynchronous Receiver/Transmitter (UART) interface to configure and receive the time information. It uses another UART interface to communicate with the observation software on the PC. The DSC receives commands and parameters from the PC to start or stop the trigger signal output. The DSC also sends the timestamp data to the PC. The trigger signal is generated by the pulse width modulation (PWM) functionality, which uses two of the hardware timer units built in the DSC. Details of the signal generation are given in **Section 2.3.4**. The generated trigger signal is outputted to the trigger output terminal and inputted to the camera.

(2) GNSS MODULE

The trigger pulses and the timestamps must be generated by an accurate time source. Because the observatories are located at high latitudes, a GNSS module was selected that supports GLONASS and BeiDou in addition to GPS. Using GNSS increases the number of visible satellites, which increases the stability of the time source. The UTC-board is required to generate up to 1,000 trigger pulses per second with a stable cadence; therefore, an accurate clock oscillator is needed to operate the DSC. Moreover, to stabilize the continuous observation, the trigger signal and the timestamps must be generated as accurately as possible even if no GNSS satellite is visible. For this purpose, the LEA-M8F (u-blox) time and frequency reference GNSS module was selected, which sends the GNSS time information to the DSC. The module also includes a voltage-controlled temperature-compensated crystal oscillator

(VCTCXO). The VCTCXO produces a reference signal of 30.72 MHz that is used as the clock of the DSC. The reference signal is adjusted (disciplined) by the synchronization manager built in the module based on the GNSS time information.

(3) VOLTAGE REGULATOR

The specification of the voltage range of the external trigger signal input of the EMCCD camera is 0.0–3.3 V. To generate the trigger signal more easily, all devices on the UTC-board were selected to operate with 3.3 V. The total current consumption was less than 500 mA, as estimated from the sum of the maximum current consumption of the devices on the board. Considering the current consumption used for I/O outside of the board, a power supply device with sufficient capacity was selected. The GNSS module and the DSC are operated by a high-frequency oscillator; therefore, the power supply must eliminate high-frequency noise such as current ripples. For this purpose, a low-noise voltage regulator integrated circuit (IC) is needed. The power supplied from a 5 V/2.0 A alternating current (AC)–direct current (DC) switching adapter was passed through an LT1963A low-noise 3.3 V regulator IC on the board to create a low-noise 3.3 V/1.5 A power supply.

(4) RS-232C INTERFACE

An interface IC was used to convert the UART serial communication signal voltage (0.0–3.3 V) built into the DSC and the RS-232C serial communication signal voltage (−12 to +12 V). To operate with a 3.3 V power source, the ADM3202 interface IC (Analog Devices) was selected. The details of the communication formats are given in **Section 2.3.1**.

2.2.2. Indicators

The internal operating status of the board can be checked with indicator LEDs on the board. When the UTC-board does not operate correctly, the cause can be identified by these LEDs.

(1) POWER LED

The power indicator LED shows that the 3.3 V output from the voltage regulator IC is correctly supplied.

(2) PPS INDICATOR LED

The PPS indicator LED is inserted parallel to the PPS signal line and blinks when the PPS signal is released correctly from the GNSS module. The PPS signal is used to start the observation sequence, as described in **Section 2.3.4**.

(3) MODE INDICATOR

The mode indicator consists of two LEDs that show the mode in which the DSC is currently running. Two types of modes are used for determining whether the DSC firmware is in the idle state for accepting any commands (idle mode) or in the observation operation (observation mode). During the observation mode, only the command to stop observation is accepted.

2.2.3. Interfaces

Five interfaces are used to connect the UTC-board to the other equipment. All interfaces were assembled with a connector fixed to the case.

(1) GNSS ANTENNA CONNECTOR

The GNSS module requires an external GNSS antenna. A coaxial cable was used to connect the U.FL connector of the GNSS module to the SMA connector fixed to the case.

(2) TRIGGER PULSE OUTPUT CONNECTOR

The trigger signal was outputted from an I/O pin of the DSC, which was connected to a SMA connector fixed on the case.

(3) POWER SUPPLY

To obtain 3.3 V output from the regulator in the circuit, it is necessary to supply power with a minimum voltage of 3.7 V and a maximum voltage of 20 V. Therefore, a small switching AC adapter (GF12-US0520, Go Forward Enterprise Corp.) with 5 V/2 A output was used.

(4) RS-232C CONNECTOR

RS-232C serial communication was used to communicate with the PC. An RS-232C connector was fixed to the case.

(5) ICSP CONNECTOR

An In Circuit Serial Programming (ICSP) connector was integrated on the board to connect the PICkit 3 writing device. In addition to writing the firmware to the DSC, the device is capable of step-by-step debugging of the firmware written to the DSC while the UTC-board is in operation. This functionality facilitates the development and debugging.

2.3. Operational design

This section explains operation of the UTC-board and provides details of the internal mechanisms.

2.3.1. Communication design

The UTC-board (DSC) communicates with the PC via RS-232C serial communication, configured with 1 stop bit, no parity, 115,200 baud, and 8 data bits. The commands and return values are ASCII characters. The various commands accepted and returned by the board are summarized in **Table 2-1**. When the DSC receives two characters “CR” and “LF” in succession, it evaluates the string held in the buffer to identify the command string. The buffer is a ring buffer of 256 bytes configured in a First-In First-Out (FIFO) manner to ensure the execution order of the received commands.

In the communication between the board and the PC, the highest communication speed is required when the time stamp is sent to the PC for each imaging frame during the observation. Therefore, the timestamps are sent to the PC in binary data to reduce the data amount and gain processing speed. The timestamp data has the form of the second of day (SOD) in the 24 bits data length and the millisecond value in the 16 bits data length, which requires 40 bits of data length. Considering the communication parameters (one start bit, no parity, and one stop bit) and 8 bits of data for one serial frame, a single timestamp data requires 5 serial frames which is 50 bits of binary length. Considering that there is no error during the data transmission, the configured communication speed of 115,200 baud can send 2,304 timestamps in 1 s. The requirement is 1,000 fps; therefore, this communication speed is theoretically 2.3 times faster than the required speed.

Table 2-1: Commands accepted by the UTC-board and their return values.

Command	Return			Description
	Type	Value		
During Idle Mode:				
PIC_CHECK	HEX	06(ACK)		Health check. Return ACK if running in the *Idle Mode* (ready to accept a command).
GPS_CHECKPPS	HEX	00|01		Whether the PPS signal is output (01) or not (00).
GPS_DEBUG	STR	"¥r¥nEntered GPS Path Through Mode¥r¥n"		Enter *GPS Path Through Mode*, which passes commands from the PC to the GPS module. Used when configuring the GPS module from PC.
GPS_SVIN	HEX	06(ACK)|15(NAK)		Send a command to the GNSS module to start the SURVEY-IN. Returns ACK if started, NAK if not.
GPS_SVVALID	HEX	00|01		Whether SURVEY-IN has been completed once (01) or incomplete (00).
GPS_SVACTIVE	HEX	00|01		Whether in the middle of SURVEY-IN (01) or not (00).
GPS_SVCHECK	HEX	00|01	00|01	Execute two commands GPS_SVVALID and GPS_SVACTIVE and return the results in order.
SET_FPS	HEX	01|02|03|06(ACK)		Set FPS value. After receiving this command, it waits 0.1 seconds for a string of 4 digits with trailing CRLF, and returns the resulting code. 01: Timeout 02: Received character was NULL or not a number 03: Not a possible value (Undividable by 15360000) 06: Success
GET_FPS	HEX	fps&0xff	fps>>8&0xff	The current fps value (16 bit) is returned in two parts, the lower 8 bits and the upper 8 bits.
OBS_START	HEX	06(ACK)		Start the observation sequence. Enter the *Observation Mode*.
During Observation Mode:				
OBS_STOP	HEX	06(ACK)		Stop the observation sequence. Exit the *Observation Mode* and return to the *Idle Mode*.
During GPS Path Through Mode:				
QUIT	HEX	06(ACK)		Exit the *GPS Path Through Mode* and return to the *Idle Mode*.

2.3.2. Reset functionality

To maintain unmanned continuous observation, several methods are designed to reset the operation of the UTC-board.

(1) Software reset

Inside the DSC firmware, after receiving the OBS_STOP command the software reset clears the serial communication buffers and re-initiates all variables so that the next observation starts from a refreshed state. This is performed automatically at the end of observation every day.

(2) Hardware reset

By changing the DTR signal pin of RS-232C from L to H, the Master Clear (MCLR) pin of the DSC is connected to GND through a photocoupler switch so that the DSC is restarted. The DSC starts from the beginning of the firmware. The GNSS module is not restarted. This is performed manually when needed by turning the DTR signal from the serial terminal software on the observation PC, which can be accessed through the internet.

(3) All reset

By cutting the power of the UTC-board off and on, both DSC and GNSS module are restarted. The satellite information is cached in the GNSS module, however the positioning and the survey-in is redone. This is performed manually when needed by controlling the watchboot power switch from the PC, which can be accessed through the internet.

2.3.3. Software

Before the UTC-board system was developed, the HAIs were controlled by “ebicam” software originally developed by Y. Ebihara. The software is written in C++ programming language. Once the ebicam starts, it reads a setting file and a schedule file and stores the values. The setting file describes the observation latitude and longitude, the threshold of the sun elevation, the directory for saving the images, and the location of the schedule file. The schedule file determines the range of observation time and camera parameters such as exposure time and EM gain. Ebicam sends the camera parameters to the camera, and waits for the start of the observation. When the sun elevation becomes lower than the threshold and the PC time is within the range of observation time, ebicam sends the start of acquisition command to the camera and waits within a loop for an image to be sent from the camera. The camera acquires an image with its internal trigger and sends it to the PC. When the image reaches the PC, ebicam adds a timestamp to the image data based on the PC time. Multiple images acquired within 1 min are stored in one file as combined raw data.

To implement the newly developed UTC-board system, the observation program required modification. At the observation start, it must send commands to the UTC-board, and during the observation, it must save the timestamp received from the UTC-board in synchronization with the image saving sequence. The observation software was modified by the author and renamed “akicam.” The detailed sequence of data acquisition is described in S**ection 2.3.4**. All commands controlling the UTC-board are designed in human-readable ASCII strings format to make trouble shootings easier in case of communication errors with the akicam software. Akicam sends the command string by appending the “CR” and “LF” at the end so that the UTC-board can recognize the end of

the command string. When the UTC-board receives a command, it returns the return value to the PC. The designed commands and return values are summarized in **Table 2-1**. The commands are sent through the RS-232C with the configuration of 1 stop bit 1, no parity, 115,200 baud, and 8 bits of data.

2.3.4. Trigger generation and timestamp association

The associations between an image and a timestamp and between a timestamp and the GNSS time must be guaranteed. The separation of triggering and timestamping functionality from the observation software enables accuracy in the timestamp but also complicates the mechanism for associating a timestamp with each image. Apart from sending commands to the camera and the board, akicam acts in a passive manner during observation to receive all image data and timestamp data. The sequence of association of the timestamp is as follows. The trigger board sends the timestamp data to the PC for each trigger pulse that was sent to the camera. The camera sends the image data to the PC for each trigger pulse. The received timestamp data on the PC will be added to a log file with the image ID on one line. If the camera fails to obtain an image and the PC receives no image data, the timestamp will be thrown away, and the next timestamp will be treated when the next image is received to guarantee the association with the last received image data.

The mechanism to generate trigger pulses based on the GNSS information is explained here. The timeline diagram of the synchronization is shown in **Figure 2-6**. The Fosc is the main oscillator frequency, which is the 30.72 MHz signal provided by the GNSS module. When the DSC receives a command to start observation (OBS_START),

it requests the time information to the GNSS module. At the next PPS timing, the DSC receives the time information of that second. Then, it prepares the timer modules and starts triggering. Two of the four 16-bit TIMER modules (T2, T3, T4, and T5) within the DSC are combined to form two 32-bit timers (T23, T45) to count the instruction cycle clock ($\mathrm{Fcy} = \mathrm{Fosc} / 2$). Both timers start counting at the same time at which the first trigger pulse is raised, then falls after every T45 counts and then raises after every T23 counts (T45 < T23). Because the DSC executes its firmware in a step of the instruction cycle Fcy, the instruction counts of T23 to raise the trigger pulse of desired fps value is calculated as

$$Instruction\ counts\ of\ T23\ = \frac{Fcy}{fps} = \frac{(30.72\times10^{6})}{2\times fps}, \tag{5.2}$$

and the instruction counts of T45 to decrease the trigger pulse is determined by multiplying the duty ratio of 0 < duty < 1. This functionality uses the trigger pulse to control the exposure time; when the Synchronous Readout Trigger Mode is used, the duty ratio is unrelated, and only the rising edge is used to end the exposure and start the next. Therefore, the duty ratio is fixed to 0.5. The PPS signal is connected to the external interrupt pin of the DSC, which makes it possible to emit an interruption in the firmware instruction every second. This signal is used to align the increase in the trigger pulse to the exact 0 sec time.

When the DSC receives a command to stop (OBS_STOP), it waits until the next fall of the trigger pulse and stops triggering, then it sends the finished signal to the PC.

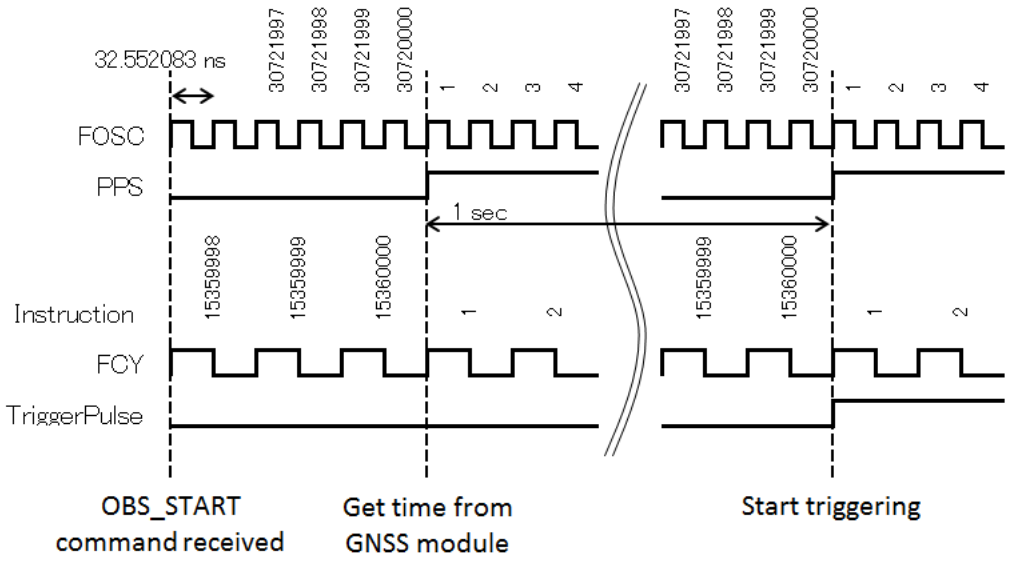

Figure 2-6: The Fosc is the reference signal from the GNSS module. The Fcy is the instruction cycle clock, which equals Fosc/2.

2.3.5. Accuracy of the absolute timestamp

In this design, no time delay due to software processing occurs between the trigger pulse and the timestamp. Two measures of time accuracy remain in the system. The first is the timing accuracy, which is the time delay between the GNSS time and the recorded timestamp of each frame. There are three measurement time delays: (1) from the rising of trigger pulse input to the beginning of the exposure, which takes up to 165.58 μs at the largest value with the Synchronous Readout Trigger Mode (Hamamatsu DCAM-API Function Reference); (2) less than 100 ns is the time delay obtained by dividing the maximum positioning error of 30 m by the light speed; (3) about 70 ns is the delay when the pulse travels 15 m of the cable up to the CMOS at a speed of 70% of the light speed.

Delay (1) is constant and correctable, while (2) and (3) are variable but small compared to the required time accuracy (= 1 ms).

The second measurement is the frequency accuracy. Because the trigger pulse is generated by counting the instruction cycle in the DSC, the frequency accuracy of the Fosc must be ensured so that it does not alter the exposure time or accumulate to time delay as a result. The frequency of the VCTCXO is corrected (disciplined) continuously within the GNSS module to account for changes in temperature (<5 ppb). During hold-over, the most recent setting is held, and the frequency stability is determined by the oscillator characteristics (<25 ppb). The disciplining continues whenever a signal from at least one satellite is received. The correction rate of disciplining is restricted to less than 30 ppb/s to stabilize the camera exposure time of each frame. The disciplining is performed by shifting the frequency so that the number of pulses of the reference signal between two PPS signals does not change. Therefore, the fluctuation is skewed to plus or minus and does not accumulate as time error on the resulting trigger pulse. Moreover, the sequence that aligns the increase in the trigger pulse to the PPS signal also ensures re-alignment of the trigger pulse to GNSS time every second.

2.4. Production

The circuit was tested on a breadboard, as shown in **Figure 2-7**.

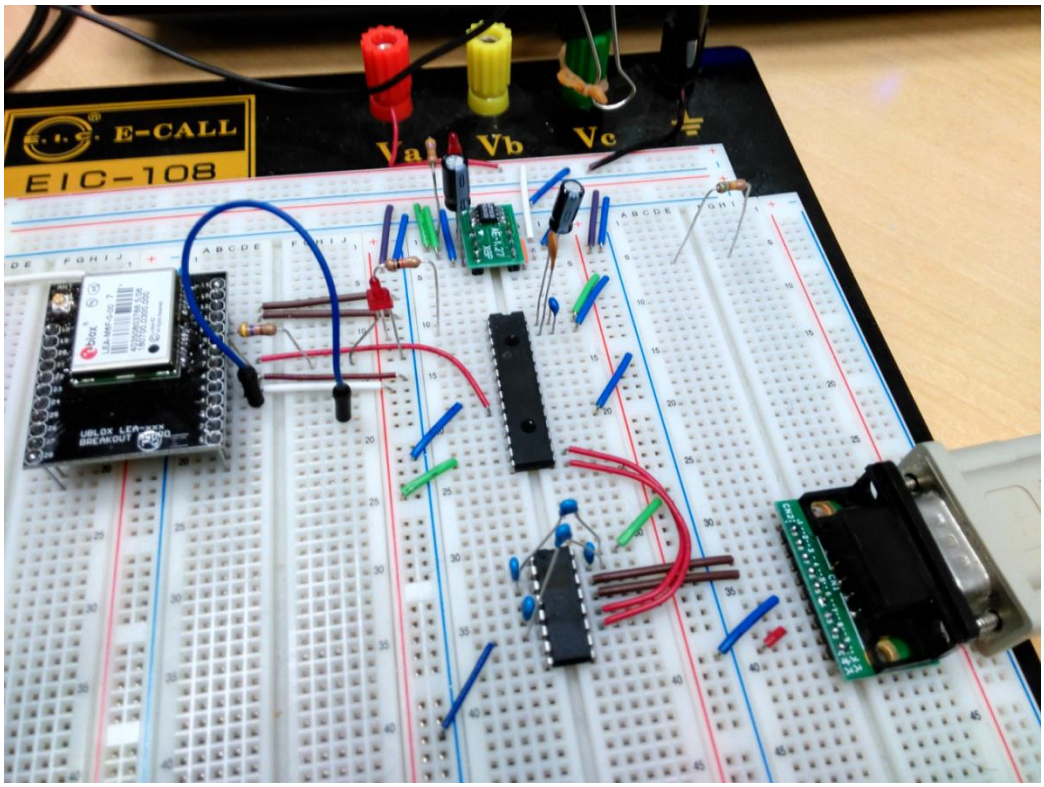

Figure 2-7: Design pattern of the UTC circuit board

The design pattern of the circuit board is shown in **Figure 2-8**, and the created UTC-board is shown in **Figure 2-9**. The design pattern was created by Printed Circuit Board Editor (PCBE) free software.

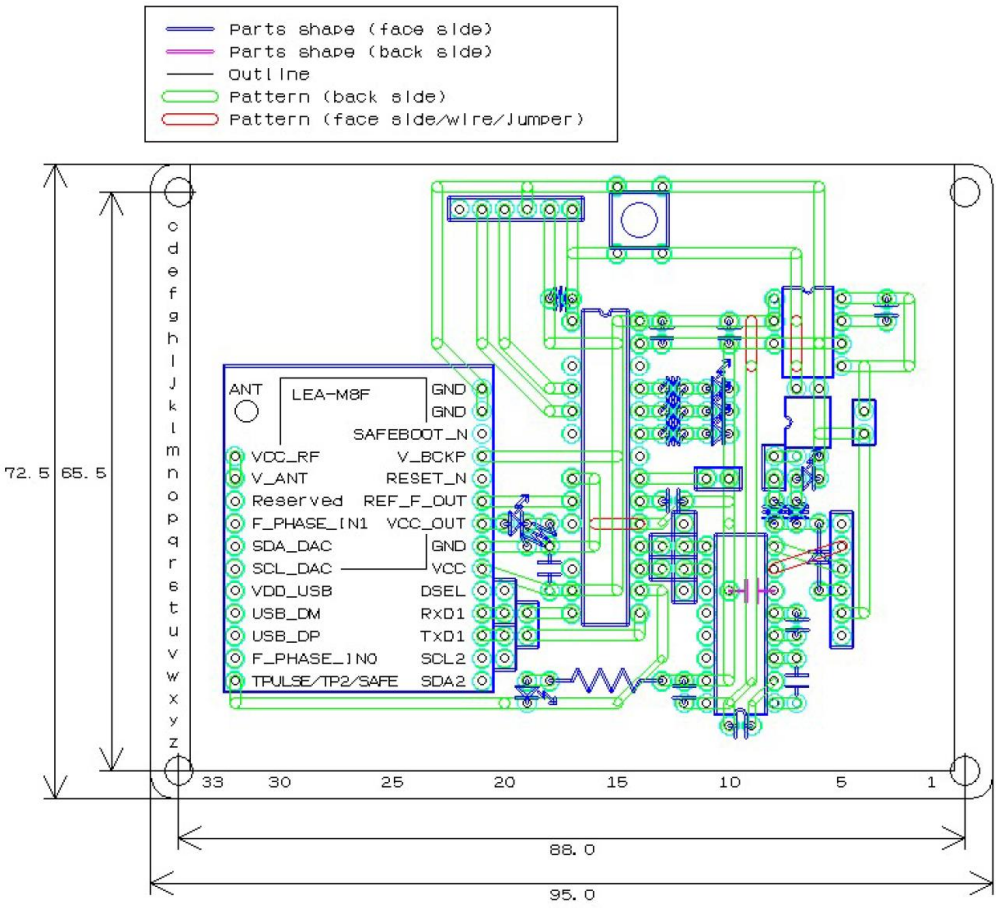

Figure 2-8: Design pattern of the UTC circuit board.

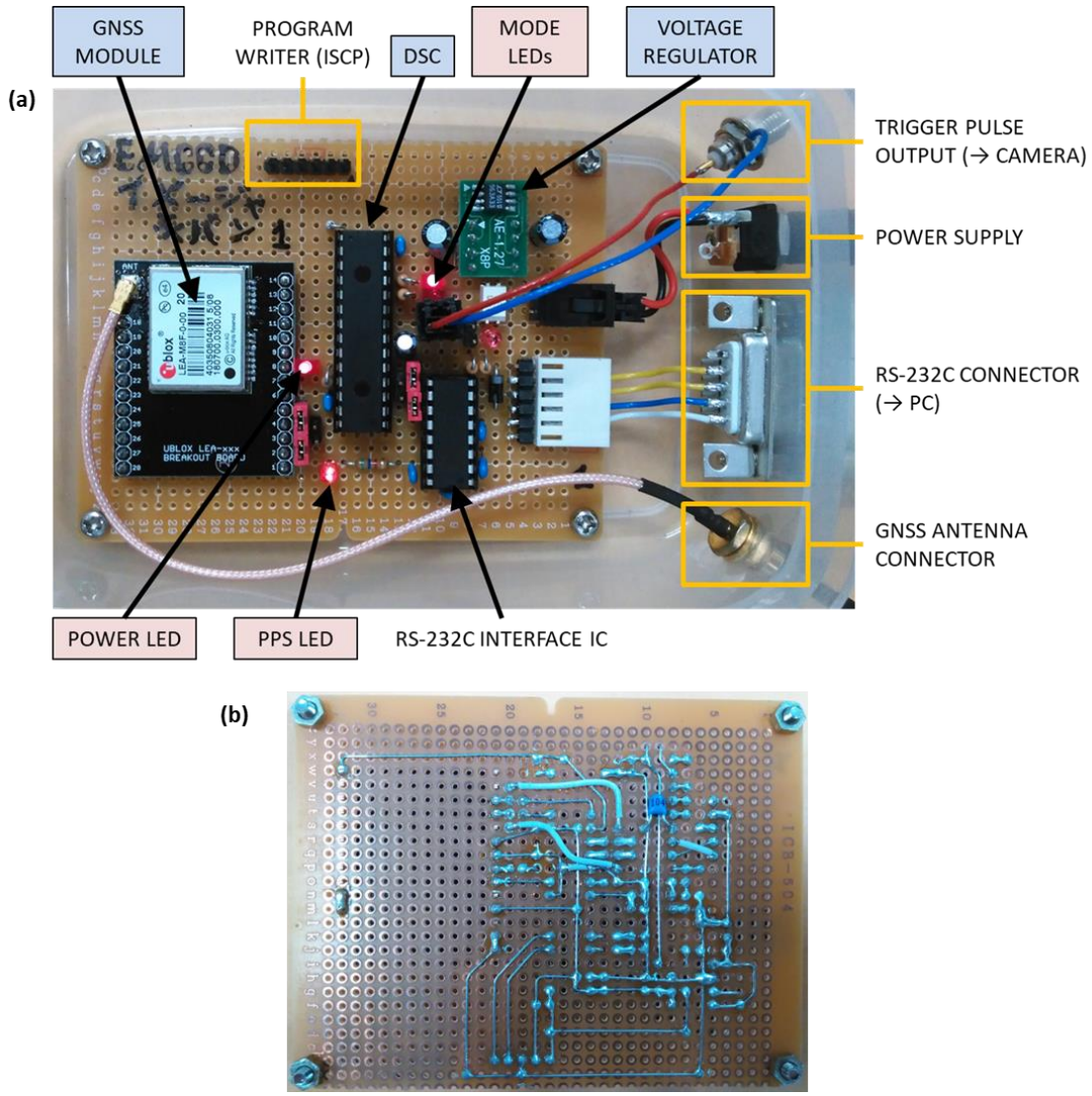

Figure 2-9: (a) Surface and (b) rear of the operating UTC-board.

3. Observation overview

Coordinated ground-based optical observations were conducted at Syowa Station in the Antarctic region (SYO; 69.00°S, 39.58°E, magnetic latitude −66.33°) and at its magnetic conjugate point Tjörnes (TJO; 66.20°N, 17.12°W, magnetic latitude 66.27°) in Iceland. Both TJO and SYO are multi-instrument facility bases. Identical all-sky imagers were installed at both locations, and a narrow FOV camera (HAI2) was also installed at SYO. The HAI2 was directing toward the magnetic zenith to identify faint and small signatures that were used for studying the fastest pulsating aurora, as discussed in **Chapter 5**. All imagers were operated at 100 fps.

Continuous observation was made for the winter seasons at TJO from September 2017 to March 2018 and from September 2018 to March 2019 and at SYO from March 2018 to September 2018. The weather conditions were acceptable, and the data coverage was approximately 86% at TJO and 87% at SYO. We obtained a total of ~100 TB of data for TJO and ~180 TB for SYO; the raw HDD were stored in the NIPR.

Several good opportunities for coordinated campaign events occurred between the Arase satellite and ground-based observations at SYO (Kataoka et al., 2019; Tanaka et al., 2019). Table 3-1 summarizes the campaign in 2018.

Table 3-1: Conjugate campaign events between ground-based HAI and the Arase satellite in 2018.

Date	Time (UT)	Conjugate station with Arase	Description
01/01 – 02/27	–	–	Arase passing time (around 10UT) is daytime.
02/27 – 05/04	–	–	Simultaneous observation period for both hemispheres. Arase passing time (around 8UT) is daytime.
06/23	04:20–05:14	Syowa	Aurorae all over the sky, pulsating in the northern half of the FOV.
07/05	19:30–22:00	Syowa	Aurora was seen.
07/06	01:30–03:00	Syowa	Light cloudy and moonlight, with a weak aurora. A bright aurora at 0237 for a moment.
07/21	01:20–01:50	Syowa	Pulsating aurora. Arase passed the southwestern edge of the FOV.
07/25	02:50–04:34	Syowa	Weak aurora, all over the sky.
08/06	23:35–02:00	Syowa	Aurora appears after 0140. At 0200, light cloudy, the aurora spreads all over the sky.
08/11	02:30–03:30	Syowa	A very weak pulsating aurora over wide area. Arase passed northeastern edge, outside the auroral area.
08/21	23:10–01:10	Syowa	Very weak aurora.
09/05	23:00–00:20	Syowa	Aurora at 23:00. Arase passes through the southwestern edge of the FOV.
	22:30–00:50	Tjornes	Sunny but no aurora.
09/22	21:20 – 00:30	Syowa	Auroral breakup. WTS.
	21:00 – 01:00	Tjornes	Auroral breakup. Eastward expanding surge.
10/07	20:50 – 23:30	Syowa	Curtain aurora.
	20:25 – 00:00	Tjornes	Cloudy.

This chapter describes and discusses the auroral substorm event occurring on September 22, 2018. This event is the best case during the coordinated campaign observations of 2017–2019 between TJO and SYO, in which the ground-based all-sky imagers successfully captured the detailed initial development of the bulge structure at the conjugate points in the Northern and Southern Hemispheres when the footprint of the Arase satellite was within the FOV of the HAIs.

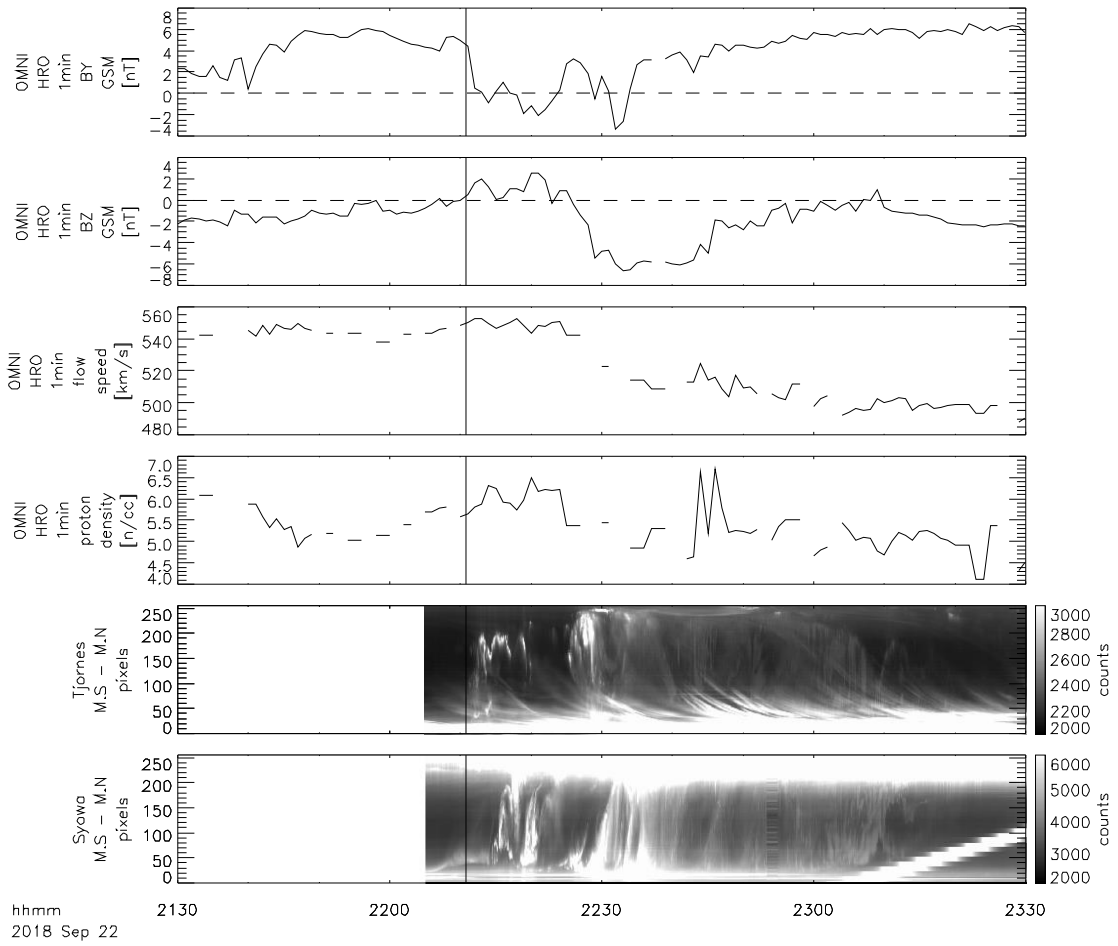

Figure 3-1: Solar wind parameters captured on September 22, 2018, as obtained from OMNIWeb. From top to bottom, IMF B_Y, B_Z, solar wind speed, and proton density are shown. The bottom two panels are keograms at TJO and SYO. The black vertical line indicates the time of the auroral onset (2210:45 UT).

The solar wind parameters and keograms at TJO and SYO are displayed in **Figure 3-1**. The solar wind data were obtained from OMNIWeb (OMNI-2). The black vertical line is the time of the auroral onset. The IMF B_Y was strongly positive before the onset.

The IMF B_Z was negative (−1 to −2 nT) before the onset. The solar wind speed was relatively high at ~540 km s^{-1}. The proton density was about 4.5–6.5 cc^{-1} during the event.

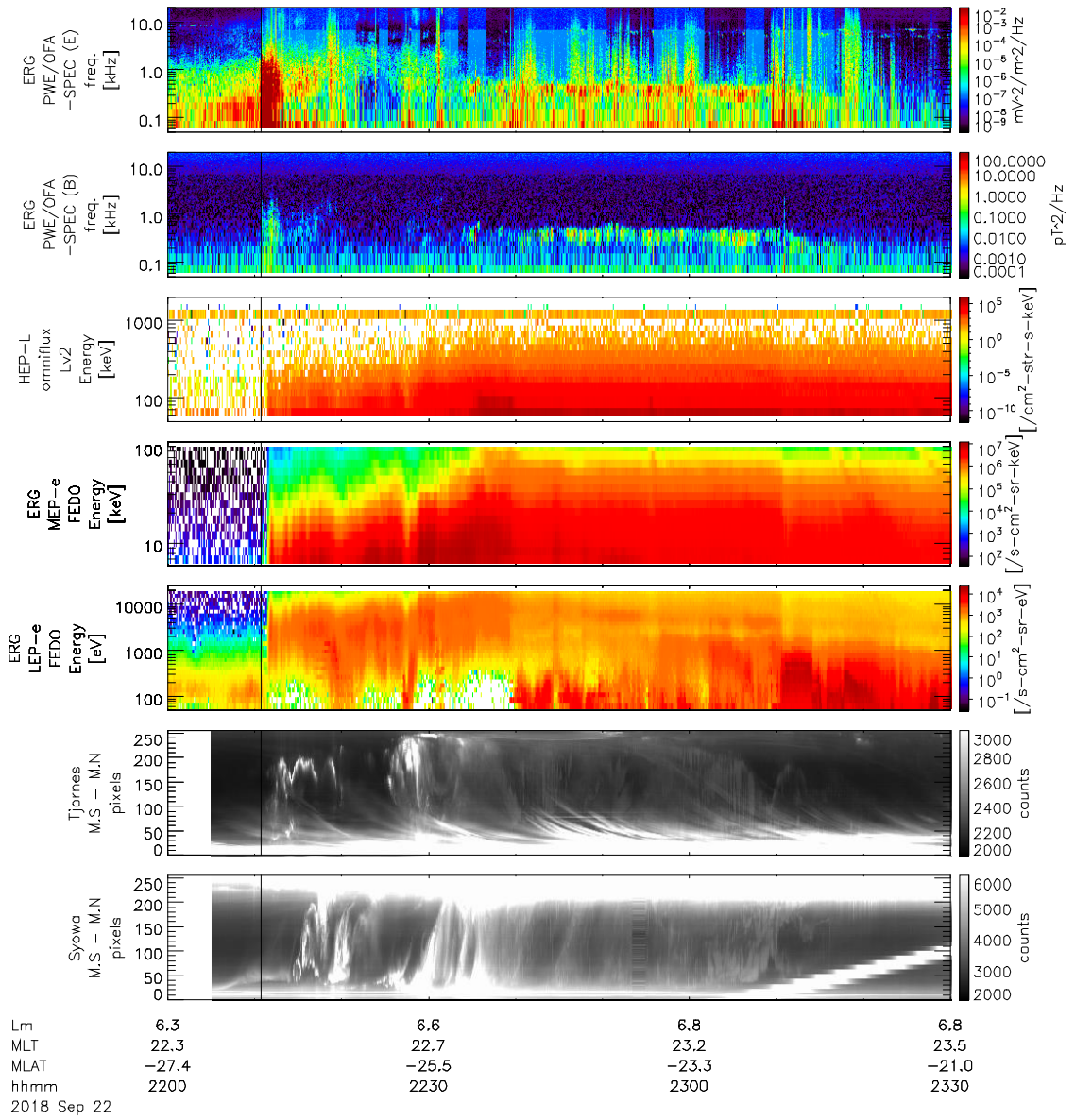

Figure 3-2: Comparison of plasma waves and electrons observed by the Arase satellite and keograms of TJO and SYO during the substorm event occurring on September 22, 2018. The black vertical line indicates the time of the auroral onset (22:10:45 UT).

The in-situ observation of plasma waves and electrons as obtained from the Arase satellite are shown in **Figure 3-2** with keograms of the HAI at TJO and SYO. The vertical axes of keograms ranging 0 to 255 are covering the viewing angle of 180°. An intensification of the aurora (initial brightening) was observed at 22:10:45 UT (onset time), and the auroral breakup was observed at both hemispheres simultaneously. The Plasma Wave Experiment (PWE) instrument onboard the Arase satellite observed a sudden pulsation associated with the substorm onset. Immediately after the auroral breakup, surge-like auroras propagated over both stations. During the recovery phase, the Arase satellite observed chorus waves, whereas pulsating auroras were observed at the ground from 22:32 UT to 23:12 UT.

The new findings on the propagating and pulsating auroras are documented in **Chapters 4** and **5**, respectively.

4. Asymmetric development of auroral breakup

4.1. Results

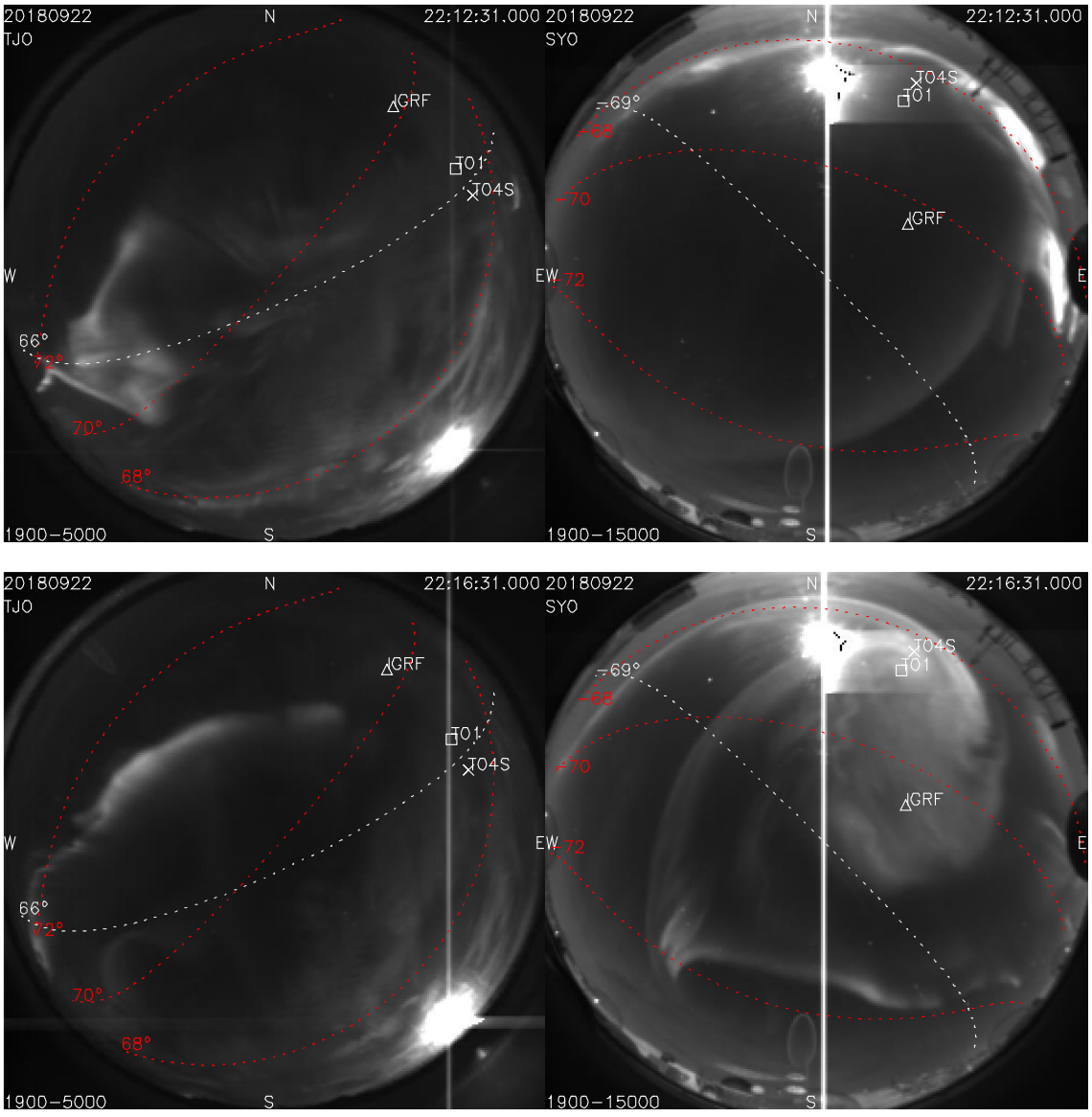

Figure 4-1: Raw all-sky images captured at 22:12 UT and 22:16 UT on September 22, 2018, when the propagating auroras expanded eastward at TJO (left) and westward at SYO (right). Geographic north is indicated at the top. The magnetic latitudes (red dotted line) and geographic latitude (white dotted line) are indicated. The triangle, square, and

cross represent the Arase footprints traced by IGRF, T01, and T04s, respectively.

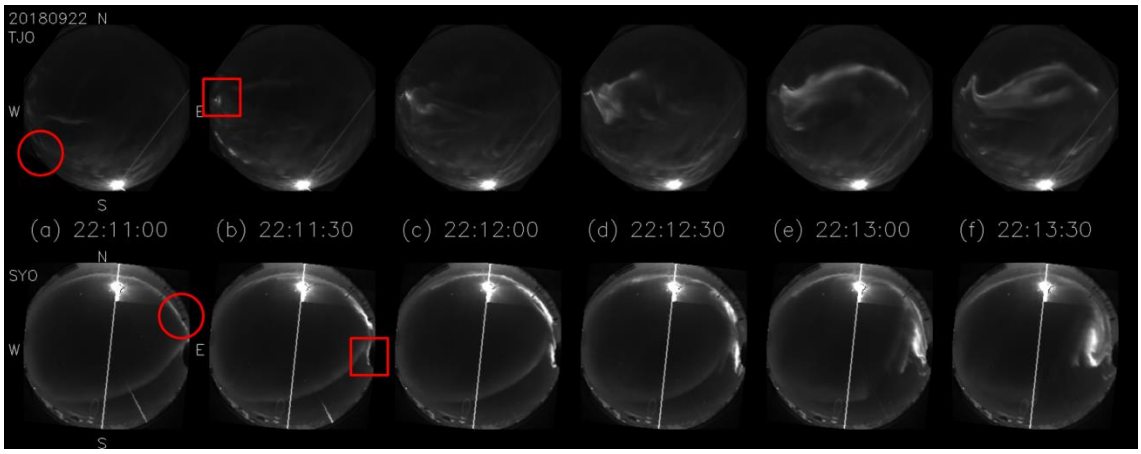

Figure 4-2: Initial brightening and development during the 2 min to show the rough temporal evolution of the propagating auroras at TJO and SYO. Geomagnetic north is indicated at the top.

On September 22, 2018, an auroral breakup and the subsequent rapid evolution of propagating auroras were simultaneously observed at magnetically conjugated points in the Northern and Southern Hemispheres. **Figure 4-2** shows the position of the initial brightening as observed by the HAIs at TJO and SYO as well as the first 2 min of the subsequent temporal evolution of the auroras.

The all-sky images were mapped to the altitude-adjusted corrected geomagnetic (AACGM) coordinate (Baker and Wing, 1989) by assuming an emission altitude of 110 km, looking downward on the ionosphere from space (**Figure 4-3a**). The coefficients of AACGM-v2 (Shepherd, 2014) were used in this study. The magnetic north is at the top, and east is to the right in both hemispheres. The initial brightening is identified in **Figure**

4-3a as blue arrows at the low-latitude side of the western (eastern) edge of the FOV at TJO (SYO) after the sudden intensification was observed at 22:10:45 UT. Then, at a higher latitude in both hemispheres, another bright auroral arc began to exhibit enhanced luminosity, as shown in the figure by red arrows.

The magnetic longitude (MLon) of the initial brightening was at 55°–60° in the Northern Hemisphere and 85°–90° in the Southern Hemisphere in the AACGM coordinate. The displacement of the initial brightening in both hemispheres was 1.7–2.3 MLT. In the Southern Hemisphere, the low-latitude structure developed at the initial brightening spot and then merged with the high-latitude aurora to form a westward traveling surge. In the Northern Hemisphere, the high-latitude and low-latitude arcs roughly maintained the latitudinal distances and were accompanied by multiple arcs between them. They propagated eastward until disappearing at 22:21:30 UT near the zenith of TJO. It is apparent that the eastward propagating aurora in the Northern Hemisphere developed more rapidly than the westward propagating aurora in the Southern Hemisphere. The propagating auroras were observed only within a few minutes after the initial brightening at the conjugate stations in the Northern and Southern Hemispheres. After the auroras traveled over the all-sky FOVs, several N–S arcs appeared during a time interval of 10 min, from 22:25 UT to 22:35 UT.

To quantitatively compare the propagation speeds, **Figure 4-3b** shows the magnetic west-to-east keograms at TJO and SYO. The vertical axes are converted to distance from the westward edge of the FOVs at the assumed emission altitude of 110 km. The average speed derived from the fitted slopes in **Figure 4-3b** is ~6.5 km s^{-1} at TJO and ~1.3 km s^{-1} at SYO.

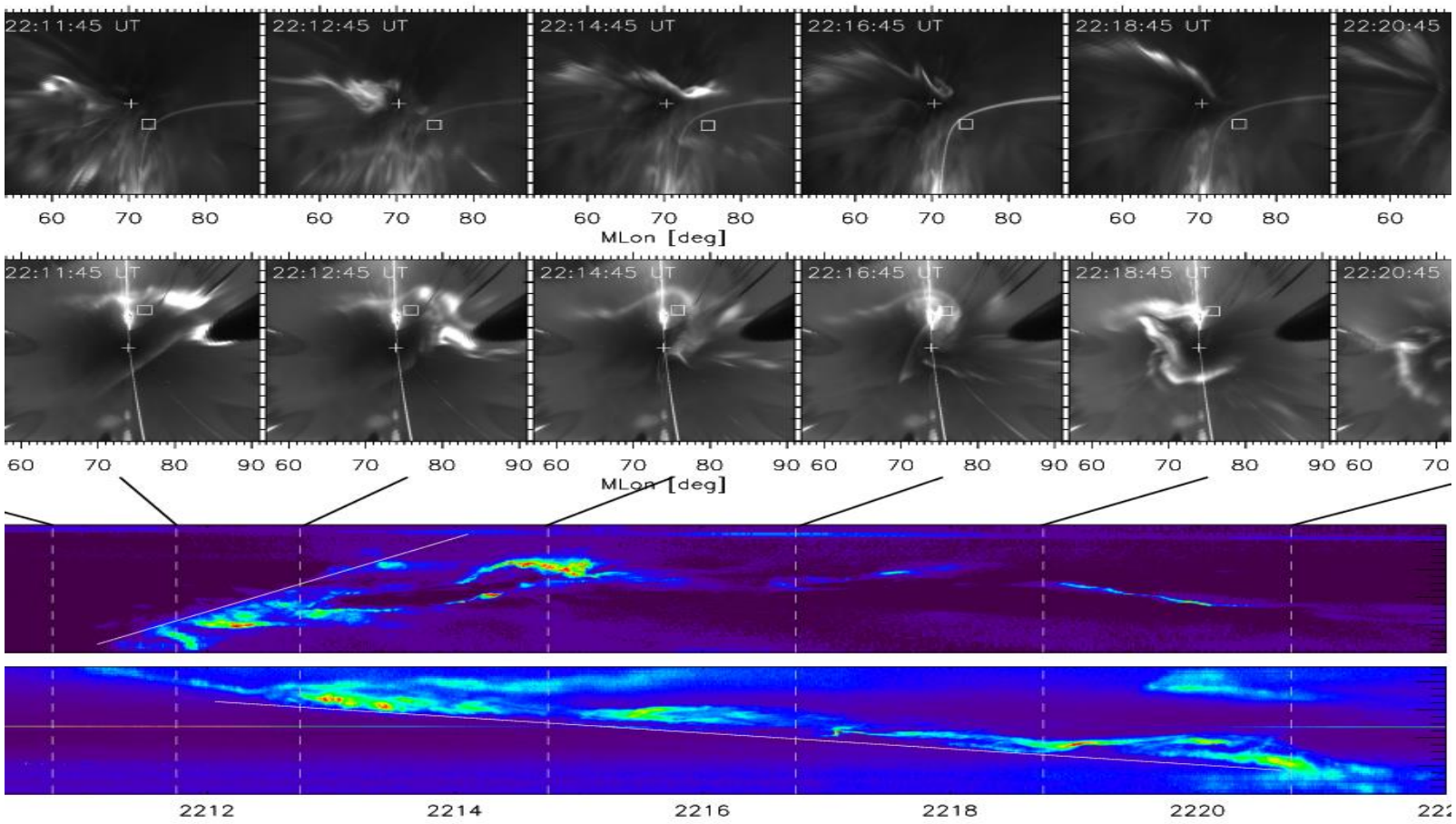

Figure 4-3: (a) First 3 min from the beginning of the aurora brightening at TJO (top panel) and SYO (middle panel) at 22:10:45 UT, and every 2 min of the subsequent evolution of the propagating auroras for 10 min. The all-sky images are mapped onto the AACGM coordinates. (b) Magnetic west-to-east keograms over the expanding aurora. The unit of the vertical axis was converted to kilometers, assuming the auroral emission altitude of 110 km.

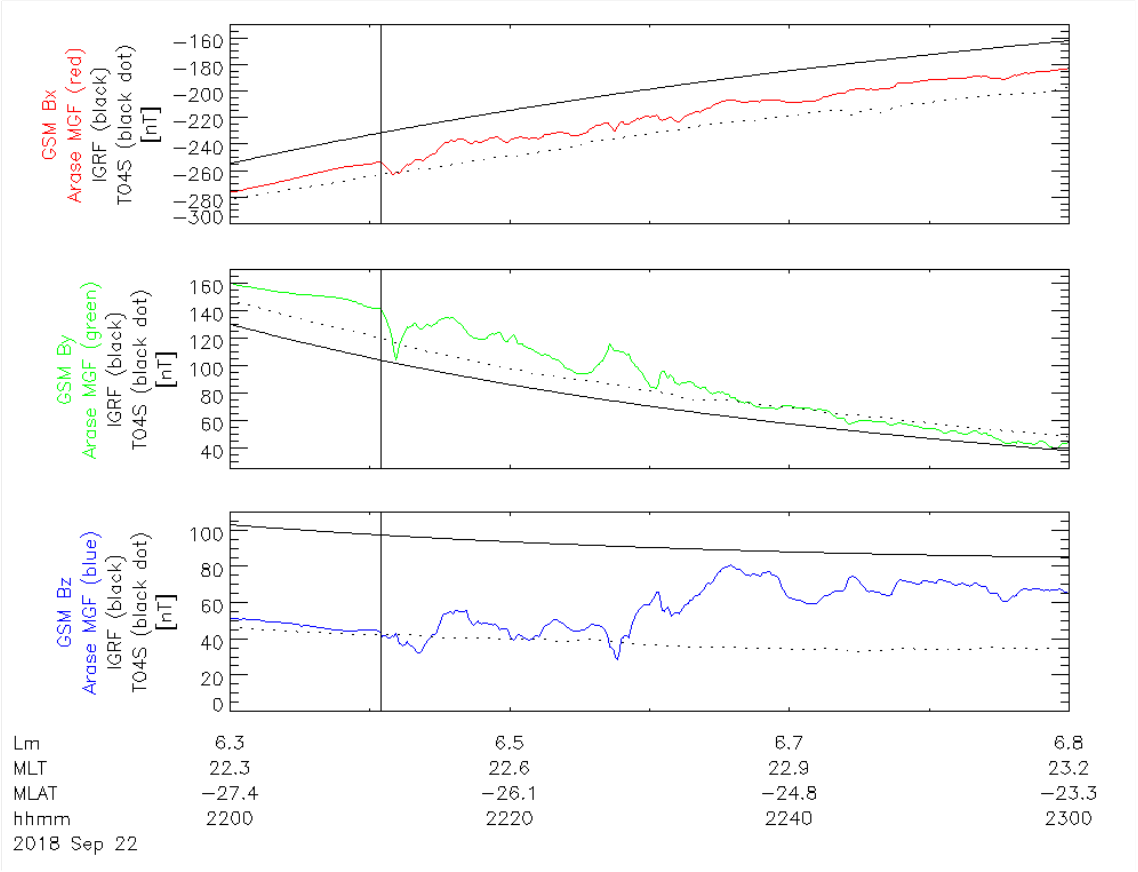

Figure 4-4: Magnetic field vectors measured by the Arase satellite for 1 h from 2200 UT on September 22, 2018. The black curves in these panels indicate the IGRF model, and the dotted lines indicate the T04s model. The vertical line indicates the timing of the auroral breakup.

The Arase satellite observed a sudden, significant disturbance in the magnetosphere in association with the substorm onset. **Figure 4-4** compares the magnetic field variations measured by the Arase satellite with data of the International Geomagnetic Reference Field (IGRF) model and the T04s model (Tsyganenko and Sitnov, 2005). The Arase satellite observed a positive excess of the B_Y component in the GSM coordinate system against the T04s before the onset time (black vertical line in the figure). The observed

excess could be associated with FACs that were not considered by the T04s model. It is also apparent that the B_Y excess present before the breakup gradually relaxed within ~30 min after the breakup.

4.2. Discussions

4.2.1. Longitudinal displacement of conjugate initial brightening

A distinctive feature of this auroral breakup event is the large displacement of the initial brightening in the longitudinal direction far from the nominal conjugate points. One of the most plausible factors causing the displacement of the geomagnetic conjugate points is the effect of the IMF B_Y. The large-scale magnetic field in the nightside magnetosphere can be twisted in the same direction as the IMF B_Y (Cowley, 1981; Østgaard et al., 2005; Saita et al., 2011), and the conjugate points themselves can shift accordingly. During the positive IMF B_Y condition, the conjugate positions are therefore expected to shift duskward or westward in the Northern Hemisphere and in the opposite direction in the Southern Hemisphere.

The substorm onset occurred close to the arrival time of the northward turning of the IMF (**Figure 3-1**). The IMF B_Y was positive, at ~5.5 nT on average, for more than 1 h prior to the brightening, which is consistent with the observed displacement of the initial brightening. The amount of longitudinal displacement of 1.7–2.3 MLT, however, is larger than the empirical formula (Østgaard et al., 2004), which gives only ~1 MLT difference if the IMF B_Y is 5.5 nT. However, such a difference from the empirical formula was not unexpected. For example, Østgaard et al. (2018) reported ~2.0 MLT events. The observed excess of the B_Y component against the modeled magnetic field, as observed by the Arase

satellite, is also consistent with the large shift of the conjugate positions in both hemispheres.

It is noteworthy that dipole tilt and seasons can also cause longitudinal displacement (e.g., Liou and Newell, 2010; Ohma et al., 2018). Because the observations were made near the equinox in this case, both of these effects can be ignored.

Other possibilities for causing the large longitudinal displacement of the initial brightening have been reported. For example, Sato et al. (1998) suggested that the triggering source of an aurora breakup could exist at an off-equator point. Morioka et al. (2011) reported that the ionosphere can control a substorm onset via the formation of auroral acceleration regions. Recently, Ebihara and Tanaka (2015a) simulated the initial brightening of an auroral breakup using global MHD simulation using the Reproduce Plasma Universe (REPPU) code (Tanaka, 2015). Their results showed that the localized enhancement of the upward FAC originated in the near-Earth off-equatorial region.

4.2.2. Asymmetric propagation

To verify the relationship between the state of the ionosphere and the asymmetric propagation of the aurora, we investigated the ionospheric equivalent current at both stations (**Figure 4-5**). Before the onset, the H-component of the magnetic field at TJO (SYO) was larger (smaller) than that of the quiet-day variation. When the propagating aurora at TJO reached the zenith, the H and D components changed signs, which likely reflects the rapid evolution of the complex current system of the auroral breakup.

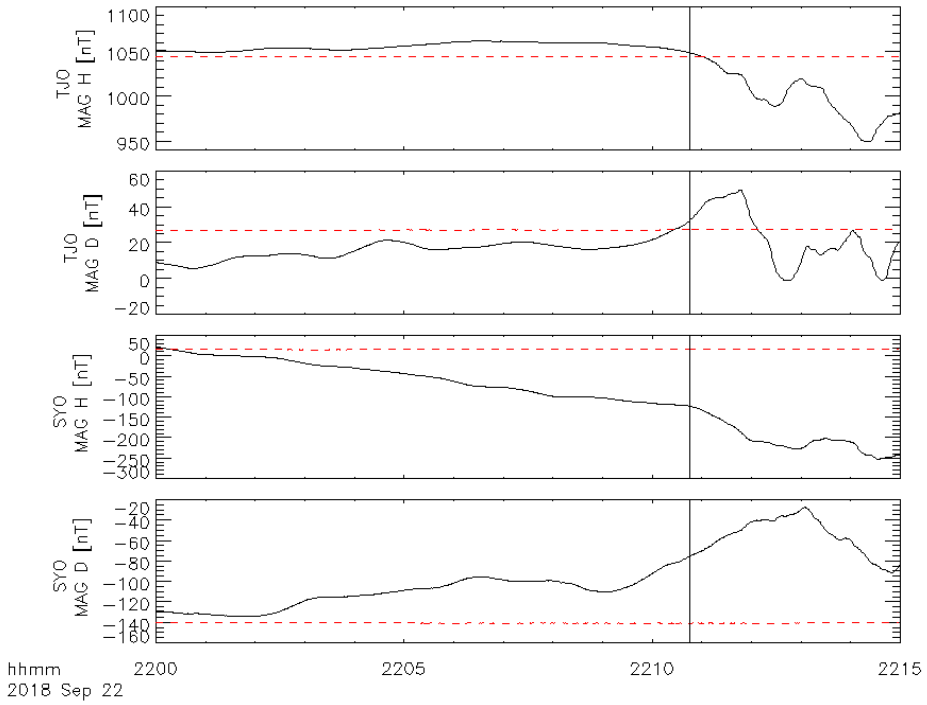

Figure 4-5: Horizontal component of ground-based magnetic field variation (H and D) at TJO (Tjörnes) and SYO (Syowa) for 15 min beginning at 22:00 UT on September 22, 2018 (solid black line). The dashed red line indicates the quiet day values observed on September 20, 2018. The vertical line indicates the timing of the initial brightening.

Figure 4-6 shows the ionospheric equivalent current derived from SuperMAG data (Gjerloev et al., 2012) at 22:10:00 UT for both hemispheres plotted in AACGM coordinates. Before the onset, the eastward Hall current was identified at TJO, whereas the direction was clearly westward at SYO. The propagating aurora began at the westward edge of the TJO FOV, where the eastward Hall current is stronger, as expected from southern Greenland. The asymmetric two-cell patterns of the Hall current are also consistent with the IMF B_Y-dependent results of a statistical study by Haaland et al. (2007). The directions of the Hall current, therefore, could be essential for causing the

eastward and westward propagations of the aurora breakup in the Northern and Southern Hemispheres, respectively.

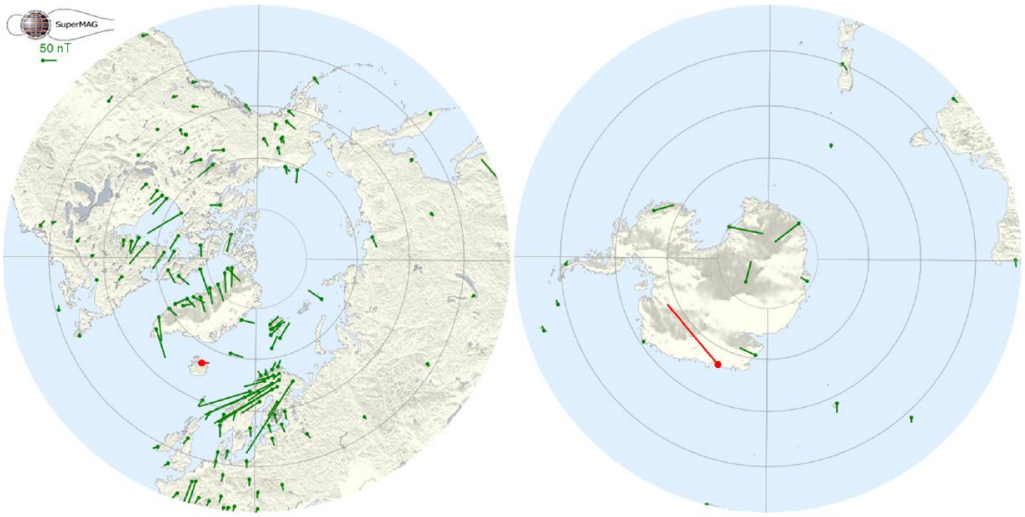

Figure 4-6: Ionospheric equivalent currents in the Northern Hemisphere (left) and Southern Hemisphere (right) obtained at 22:10:00 UT, as derived from SuperMAG data. Top of the image is toward the sun, and the right side is dawn. The Southern Hemisphere is viewed from the north through the Earth. The equivalent currents at TJO and SYO are superposed at twice the enhancement as that of the SuperMAG data.

For simplicity, we assumed that a similarly distorted global magnetic field continued for 30 min, as expected from **Figure 3-1**, because it was originally manifested by the initial brightening. If the mesoscale bulge structure always expands both eastward and westward (e.g., Nakamura et al., 1993), it would be natural to see an eastward propagating aurora in the Northern Hemisphere and a westward traveling surge in the Southern Hemisphere during the positive IMF B_Y-condition, as illustrated in **Figure 4-7**.

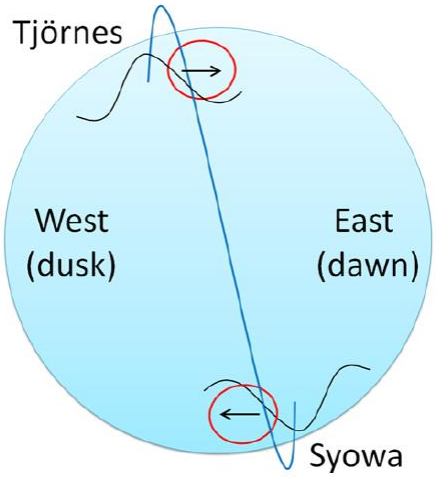

Figure 4-7: Schematic illustration of a poleward expansion in the Northern and Southern Hemispheres. The Earth is viewed from midnight toward the Sun, and dawn is to the right. The blue curve depicts the magnetic field line connecting the conjugate stations. The red circles are the FOVs of the ground-based all-sky imagers, and the arrows represent the direction of the auroral expansion.

Craven and Frank (1985) reported that after the initial brightening, a second intensification adjacent to the prior one propagates eastward. This phenomenon is similar to the eastward propagating structure in the Northern Hemisphere, as shown in **Figure 4-3a**. Such a fine auroral structure, however, could not be fully resolved by the satellite imaging of the previous study. Tanaka et al. (2015) reported observational examples that showed similar development of an eastward-expanding auroral surge in the post-midnight sector at a large distance from that of the initial brightening. The present event occurred in the pre-midnight sector near the initial brightening, and the observed propagating

auroras were in the initial stages of bulge evolution. Liou et al. (2006) also reported that an eastward-expanding auroral bulge does not clearly exhibit a surge-like structure. In our observations, the eastward propagating aurora in the Northern Hemisphere differed significantly from the typical appearance of a westward traveling surge in the Southern Hemisphere.

The scenario above, however, might be too simplified. Notably, we observed no westward (eastward) traveling structures in the Northern (Southern) Hemisphere in the initial stage of a several minutes. These results are similar to the observational report of Tanaka et al. (2015) such that no westward traveling surge was recognized in their eastward expanding events. Therefore, it can be expected that with a limitation of the best effort of ground-based all-sky imaging FOVs, the bulge structure development was dominant only in the eastward (westward) direction in the Northern (Southern) Hemisphere. Such a concept of full asymmetric propagation of the mesoscale bulge structure is consistent with the results obtained by Ebihara and Tanaka (2015b; 2018), who simulated a westward traveling surge through global MHD simulation. They showed that the propagation direction of the traveling surge is controlled by the ionosphere, and they confirmed that the direction of the surge development is not necessarily to the west but should be the same as the direction of the ionospheric Hall current.

The conjugate observation results presented in this study therefore support the possible role of the ionosphere in controlling the major auroral evolution. However, we cannot completely rule out another possibility, as shown in **Figure 4-7**, because of the limited all-sky FOVs. The effort is ongoing to distribute several all-sky imagers longitudinally in conjugate areas, which will be able to differentiate between the above two scenarios.

4.2.3. Shear at the leading edges

In this sub-section, the shear motions found in the propagating auroras are examined, assuming that the optical flow of the auroras approximately represent the plasma motion in the acceleration region (e.g., Chaston et al., 2015).

Figures 4-8 and **4-9** show shear motion in the propagating aurora recorded at TJO and SYO, respectively. The images were mapped onto the ionospheric plane at an altitude of 110 km in the direction of looking downward on the ionosphere. The three keograms are the time series along the position marked in each image (cuts 1, 2, and 3). These cuts are about 80 km apart at an altitude of 110 km. The aurora is propagating in the direction from cut 1 toward cut 3 in both hemispheres. Cut 2 is located at the leading edge of the propagating aurora, and cut 3 is in a position ahead that has not yet been reached by the bright aurora. The eastward propagating aurora at TJO shows clockwise (CW) motion. Although the westward propagating aurora at SYO shows the opposite direction on the image, the rotation is CW if viewed along the magnetic field line, which is the same direction as the rotation at TJO. Hereinafter, CW and counterclockwise (CCW) refer to the direction of rotation when viewed in the direction of the magnetic field lines.

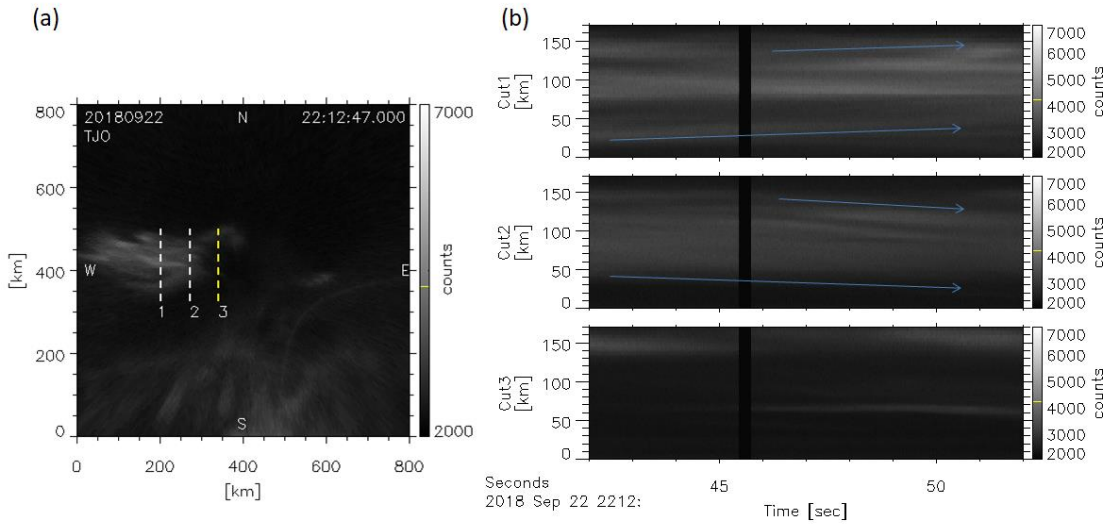

Figure 4-8: Shear motion observed in the propagating aurora at TJO. (a) The image is mapped onto a sphere at an ionospheric altitude of 110 km in the direction looking downward on the ionosphere. (b) Keogram at positions 1, 2, and 3 shown in image (a). The black vertical lines in the keogram are missing image frames.

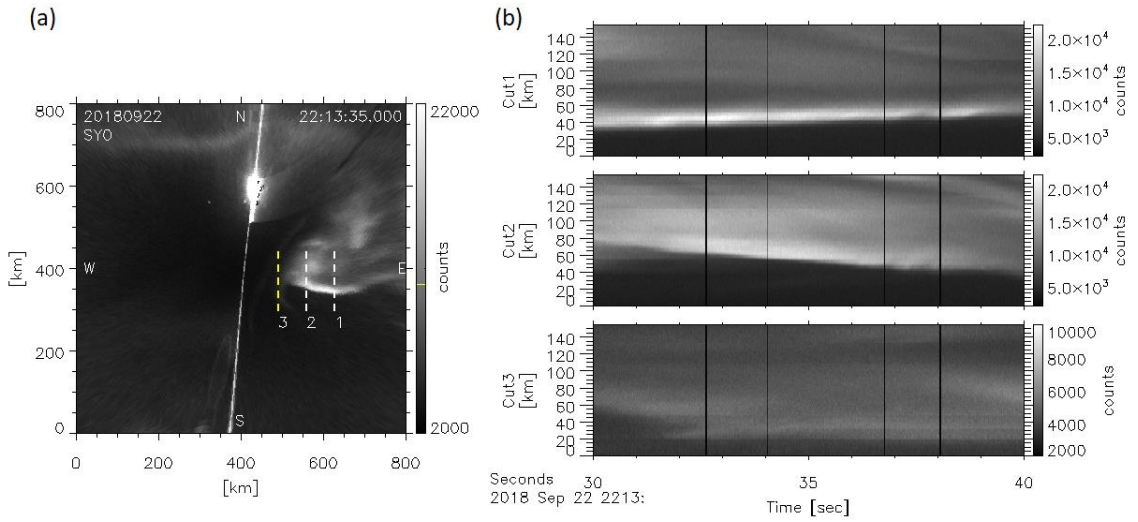

Figure 4-9: Shear motion observed in the propagating aurora at SYO. The format is the same as that discussed in Figure 4-8.

Ebihara and Tanaka (2015b; 2018) showed that both the convergence of the Hall current and the divergent electric field (CCW flow vorticity) appeared at the leading edge of the surge. However, the observed propagating auroras showed CW motion at the bright aurora area (between cuts 1 and 2) in both hemispheres, which is opposite the results of Ebihara and Tanaka (2015b; 2018). It is interesting to note that if we focus on the shear motion at the very edge of leading front (between cuts 2 and 3), the shear motion is CCW in both hemispheres. It can therefore be observationally expected that the divergent electric field is located at the very edge of the leading front of the propagating aurora, to which the aurora is about move.

Several possibilities can explain this discrepancy between the results of MHD simulation and our observation. First, the ionosphere and the inner boundary of the magnetosphere (3.0 Re) is connected directly in the MHD simulation, which could essentially lack the observed shear motion occurring in the auroral acceleration region. Second, although the MHD simulation was performed with the highest resolution at level 7, the spatial resolution might be still insufficient for reproducing the small-scale (<100 km) structure occurring at the leading edge. Improved resolution (level 8 or more) will solve this problem in future. Third, the actual plasma convection at the ionosphere might be significantly different from the observed optical flow. This point will be investigated in detail by comparing the SuperDARN observation with HAI data.

5. Rapid pulsation

5.1. Results

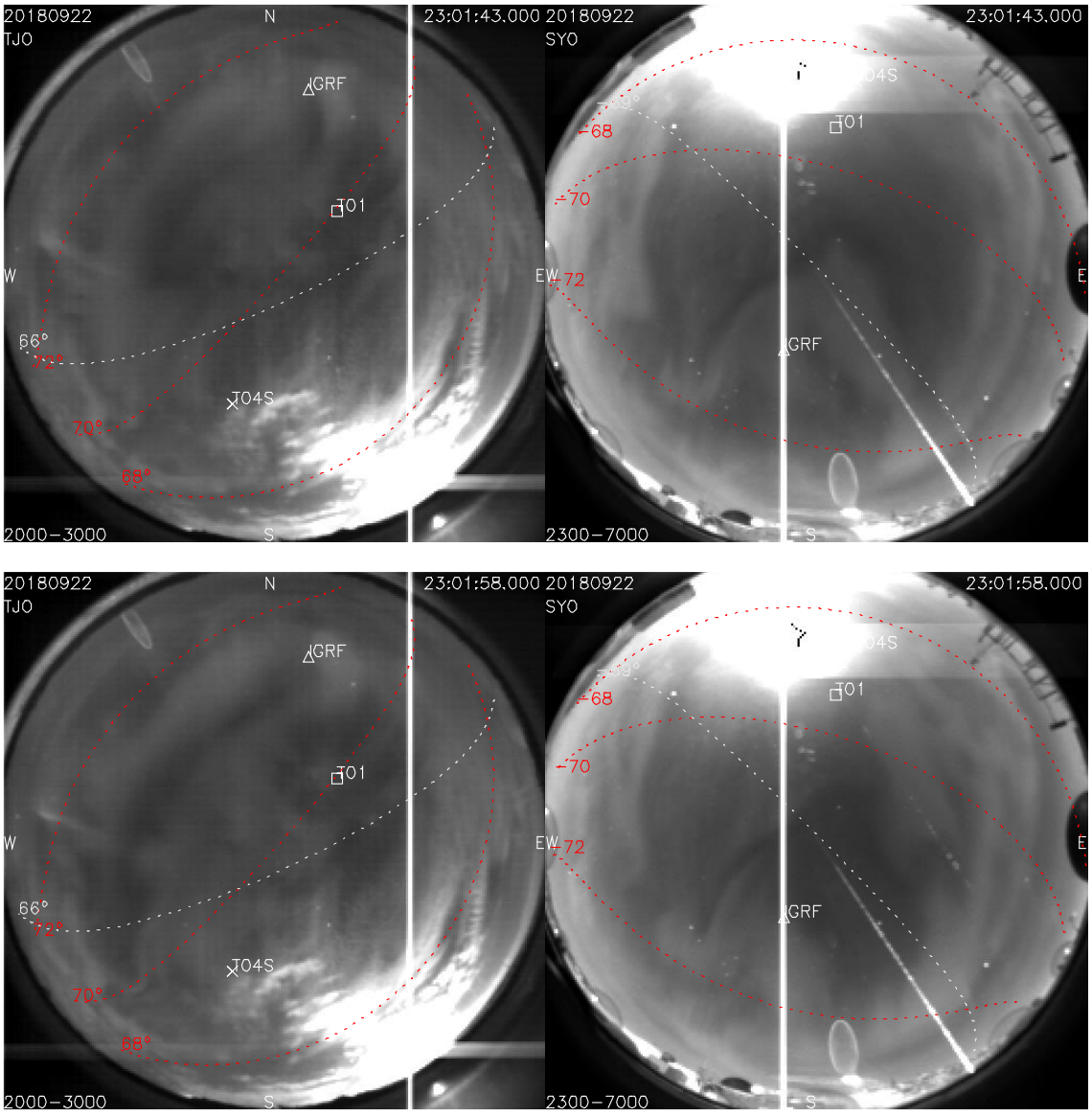

Figure 5-1: Example of the diffuse patchy auroral form during the recovery phase. These auroras are pulsating auroras. The format is the same as that discussed in Figure 4-1.

After the auroral breakup, a bright arc aurora extended in the magnetic N–S direction appeared at 22:22 UT, from the east and extended into the FOV in both hemispheres. After 10 min, at 22:32 UT, it became a very dark diffuse aurora at TJO, whereas a brighter diffuse aurora appeared over SYO. After 22:32 UT, about 20 min after the auroral breakup, diffuse and patchy pulsating auroras appeared in both hemispheres. **Figure 5-1** shows all-sky images of TJO and SYO captured at 15 s intervals. A pulsating aurora patch first appeared in the all-sky FOV at 22:32 UT at TJO and at 22:36 UT at SYO. It was difficult to find the very first patch appearing at SYO owing to the bright diffuse aurora in the background. The pulsating aurora patches that first appeared were common in both hemispheres in that the spatial size was small, at ~20 km at an altitude of 100 km, and disappeared after repeating the pulsation several times during a period of several seconds to several tens of seconds. After 22:38 UT, the main pulsation began in both hemispheres. The spatial size of the patch evolved to approximately 50 km; the periodicity of the pulsation became clearer; and the duration of the same pulsating patch increased to several minutes.

Correlation between the main pulsation and chorus wave activities was found as shown in **Figures 5-2** to **5-5**. As indicated by the white arrows in **Figures 5-2** and **5-3**, the pulsating aurora at TJO showed good correlation between the chorus wave intensity variations. Theoretically, the electrons are accelerated in a direction opposite that of the traveling direction of the chorus waves. Because the Arase satellite was located in the Southern Hemisphere, these results are consistent with those reported in previous studies (e.g., Miyoshi et al., 2015).

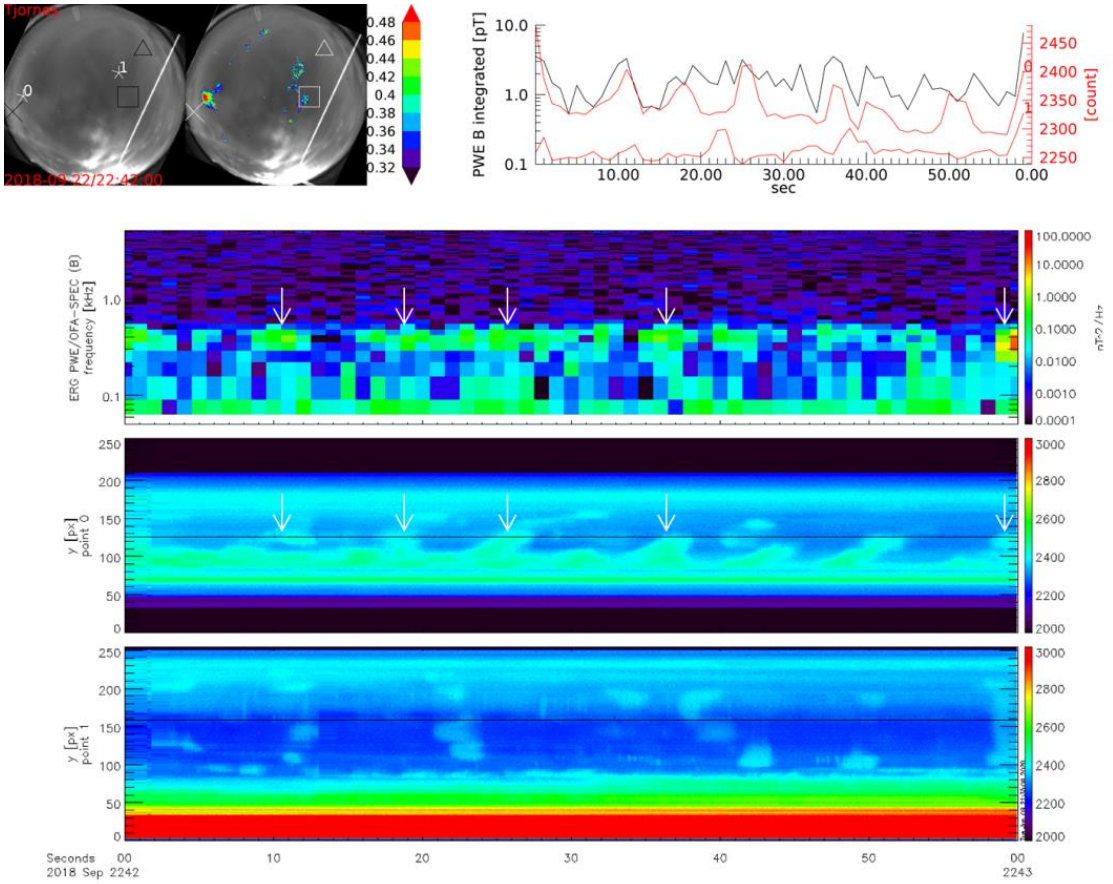

Figure 5-2: Example of one-to-one correspondence between the main pulsations at TJO and chorus wave activity observed by the Arase satellite. In the upper left image, two all-sky images are shown overplotted with several regions of interest (ROIs) and the correlation map against the intensity variation of the chorus waves. The triangle, square, and cross represent the Arase footprints traced by IGRF, T01, and T04s, respectively. The upper right panel compares the brightness curves at the ROIs (red) and the time variation of chorus wave intensity (black). The bottom three panels show the dynamic spectrum of magnetic field fluctuation observed by the Arase satellite PWE/OFA and magnetic N–S keograms crossing the ROIs.

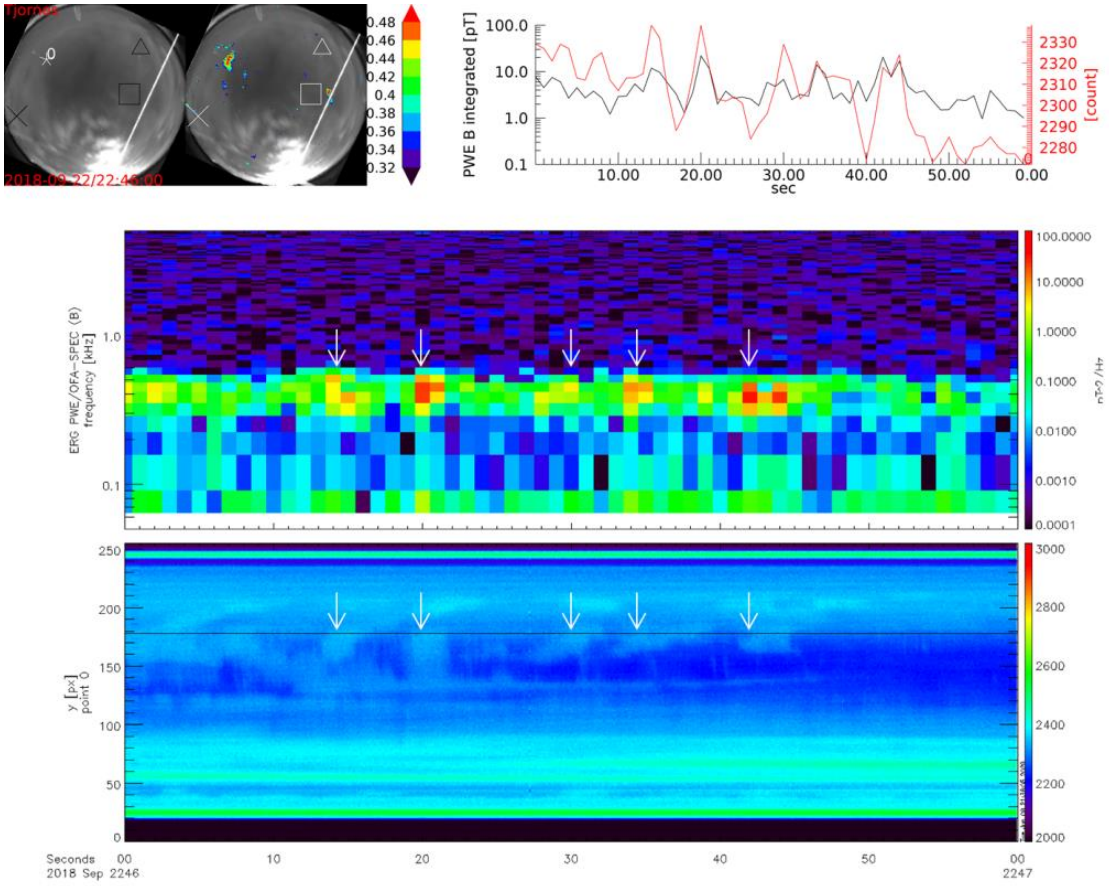

Figure 5-3: Additional example of the one-to-one correspondence between the main pulsations at TJO and chorus wave activity observed by the Arase satellite. The format is the same as that discussed in Figure 5-2.

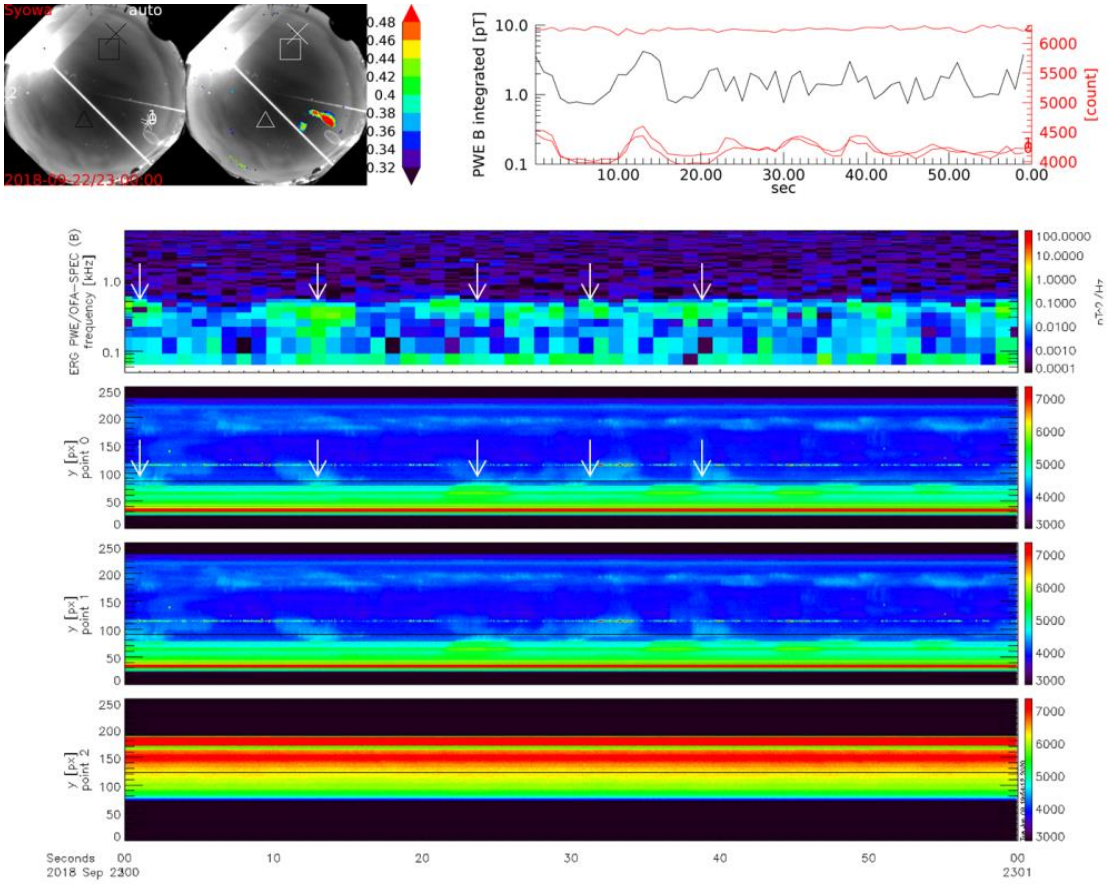

Figure 5-4: Example of the correlation between the main pulsations at SYO and chorus wave activity observed by the Arase satellite. The format is the same as that in Figure 5-2.

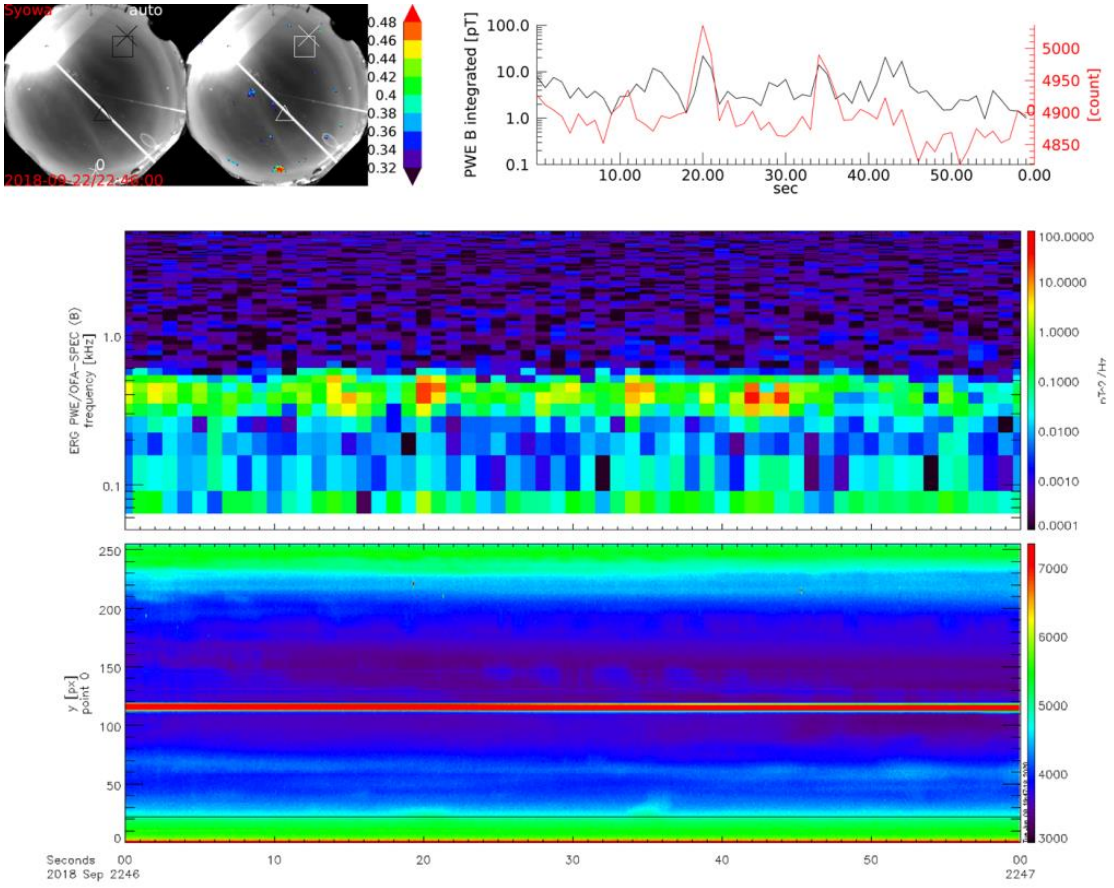

Figure 5-5: Additional example of the correlation between the main pulsations at SYO and the chorus wave activity observed by the Arase satellite. The format is the same as that discussed in Figure 5-2.

The time stamp for auroras in the Southern Hemisphere also shifted for 1 s because it takes ~1 s for the electrons precipitating into the Southern Hemisphere which are scattered from the Northern Hemisphere by a similar chorus wave.

Surprisingly, 1 min before the main pulsation began, a rapid temporal variation in auroral luminosity was observed within the narrow FOV of HAI2 without the main pulsation, in association with the chorus elements. The HAI2 points to the magnetic zenith. The spatial size of the narrow FOV is 7.72 km at 100 km altitude, which is about the same as that of a typical single pulsating patch. **Figure 5-6** shows a correlation between the

aurora observed at SYO and the lower-band chorus intensity. The lower panels compare the keograms of a selected area within the all-sky images and the narrow FOV images. The region of interest is depicted in **Figure 5-7**. At 22:34:57 UT, an aurora modulated at ~3 Hz without main pulsation appeared in the narrow FOV of HAI2.

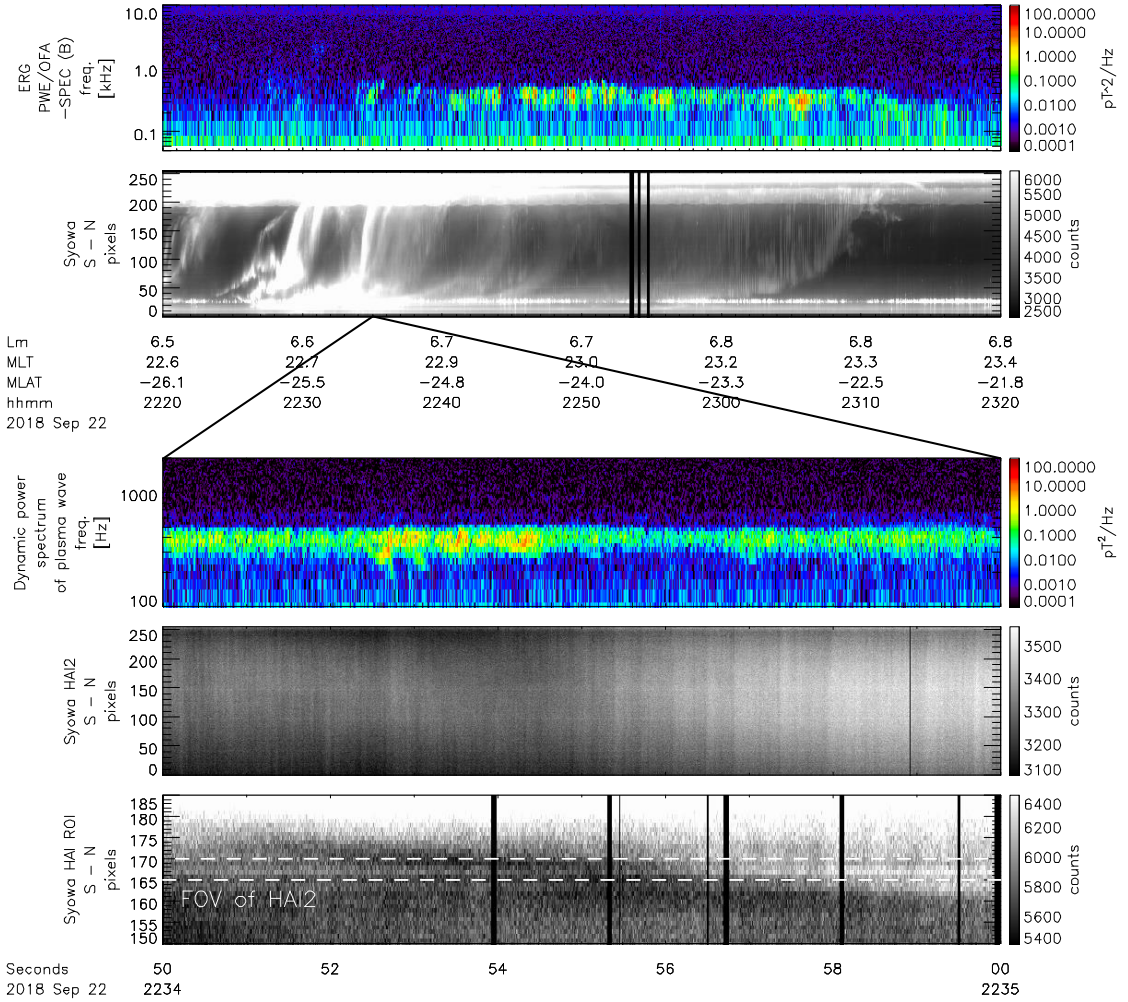

Figure 5-6: Comparison of the dynamic spectrum of the chorus waves observed by the Arase satellite with the keogram of the all-sky HAI at SYO (top two panels). The bottom three panels compare the dynamic spectra of the chorus wave expanded for 10 s beginning at 22:34:50 with the keogram of the narrow FOV of HAI2 and the keogram of an ROI

within the all-sky image. The white dotted horizontal line within the keogram indicates the region of the narrow FOV of HAI2.

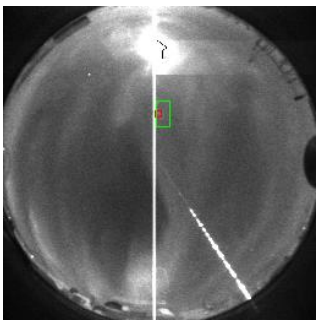

Figure 5-7: All-sky HAI image with the selected area indicated by the green square; the red square indicates the FOV of the HAI2.

At 22:34:48, just before the so-called 3 ± 1 Hz modulation appeared in the auroral intensity, ~20 Hz modulation was detected by the narrow FOV camera. **Figure 5-8** compares the dynamic spectrum of the chorus waves observed by the Arase satellite and the mean intensity variation in the HAI2 when the rapid variation occurred. The auroral intensity variation continued for ~10 s. It is apparent that variation in both the chorus wave intensity and the auroral intensity included a modulation at ~20 Hz.

Note that the footprint of the Arase satellite does not exist in the narrow FOV of HAI2. Therefore, a one-to-one correspondence could not be expected between the 20 Hz modulations observed in the intensity variations of the chorus waves and the pulsating aurora. Nevertheless, we found similar rapid variation in those, suggesting the possibility that the rapid auroral modulation could have been generated by the chorus wave.

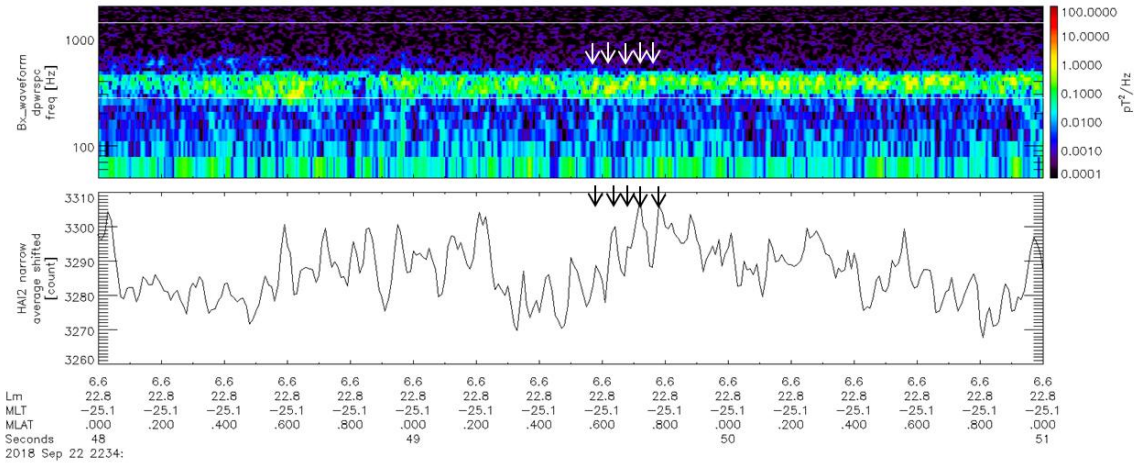

Figure 5-8: Dynamic spectra of chorus waves and variations in aurora intensity captured by the narrow FOV of HAI2. The arrows indicate the repetitive intensity variation in both the chorus wave and the aurora.

5.2. Discussions

5.2.1. Resonant energy

The precipitating electron energy can be evaluated using standard theories of resonant energy of electrons against whistler-mode waves. The resonant energy, E_R, at the first-order cyclotron resonant scattering given by Kennel and Petschek (1966) is

$$E_R = \frac{B^2}{2\mu_0 N}\frac{f_{ce}}{f}\left(1-\frac{f}{f_{ce}}\right)^3 \tag{5.1}$$

where N [m^{-3}] is the number density, B [nT] is the magnetic field strength, f is the wave frequency, and f_{ce} is the cyclotron frequency of electrons. Assuming a typical trough

density of 10 /cc at L = 5–6 (Sheeley et al., 2001) with the magnetic field strength of 100 nT at the Arase satellite of 220 nT, the resonant energy becomes ~200 keV at 300 Hz. This suggests that the electron energy was sufficiently high that the time-of-flight effect can be neglected to cause the rapid modulation of 20 Hz in the auroral intensity.

5.2.2. Possibility of subpacket

Previous research has shown that the 3 ± 1 Hz internal modulation of auroral intensity appearing in the pulsating aurora patch has a one-to-one correspondence with the chorus element (Hosokawa et al., 2020). Santolik et al. (2004) reported a fine structure of chorus wave packets obtained by Cluster spacecraft observation and referred to as subpackets. These subpackets are embedded in chorus elements when shown in a time–frequency diagram, and their time scales are less than 40 ms (Santolik et al., 2014). This time scale corresponds to that of the chorus intensity variation observed in the present event.

Figure 5-9 shows the dynamic spectra calculated from waveform data in a different time resolution at the same period as that of the last 2 s shown in **Figure 5-8**. While the lower resolution (top) panel shows a more likely rising tone in the chorus element with a duration of ~200 ms, the higher resolution (bottom) panel show a repetition of chorus elements of 50 ms duration, as denoted by white arrows in the figure. It is difficult to differentiate a subpacket from the burst repetition of chorus elements in this single example.

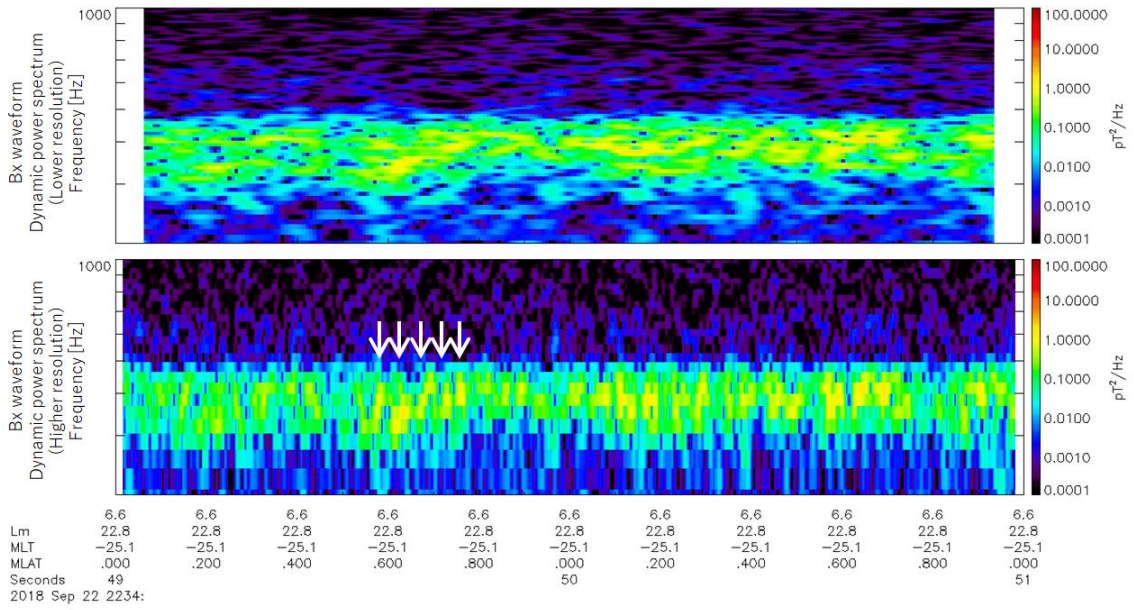

Figure 5-9: Dynamic spectra of chorus waves calculated with lower (top) and higher (bottom) time resolution. The arrows indicate the repetitive intensity variation.

6. Discussion

6.1. Brief summary

Development of high-speed imagers discussed in this study can be briefly summarized as follows: Two EMCCD all-sky camera systems were developed and installed at SYO and TJO. No optical filters were used to achieve the high-speed imaging. The resolution was 256 × 256 pixels, and the sampling rate was fixed at 100 fps. The total amount of data obtained thus far is ~100 TB for SYO (from February to September 2018) and ~100 TB for TJO (from August 2018 to March 2019). In addition, a panchromatic narrow-FOV imager was developed and installed at SYO in 2018. The total amount of HAI data obtained is ~280 TB (from February to September 2018).

New scientific findings can be briefly summarized as follows: From the campaign observation with the Arase satellite, new findings were obtained for both poleward expansion and pulsating auroras owing to the high-speed imaging. In this research, asymmetric development of the poleward expansion in the northern and southern conjugate points was identified for the first time. The results support the possible role of the ionosphere in controlling the major auroral evolution. The shear motion observed at the bright area in the propagating aurora was in an opposite sense to the results of the MHD simulation with the highest resolution, however, the same sense of shear motion was identified at the very edge of leading front. This suggests the possibility of a new understanding of the FAC connection with the substorm surge and that the spatial resolution of the simulation requires further improvement. Another new finding is about the cause of the rapid pulsation at >20 Hz, which is well beyond the ~3 Hz modulation.

This rapid pulsation is associated with the repetition of chorus elements or the subpacket.

6.2. Future directions

The detailed analysis in this thesis was focused and limited to the rapid morphological development of poleward expansion and pulsating auroras that occurred during the campaign event. Thus, several other points remain for discussion. First, scientific studies with the HAI data can be conducted without using the Arase satellite. Other than the campaign events with the Arase satellite, several other events showed rapid auroral variation in both the Northern and Southern Hemispheres. For example, as shown in **Figure 6-1**, very similar isolated auroral patch structures were found at the northern and southern conjugate points. These similarly shaped structures appeared at the same time and extended along the magnetic N–S detection, although the patch in the Northern Hemisphere was visible longer than that in the Southern Hemisphere. More detailed analysis is needed to analyze these transient auroras.

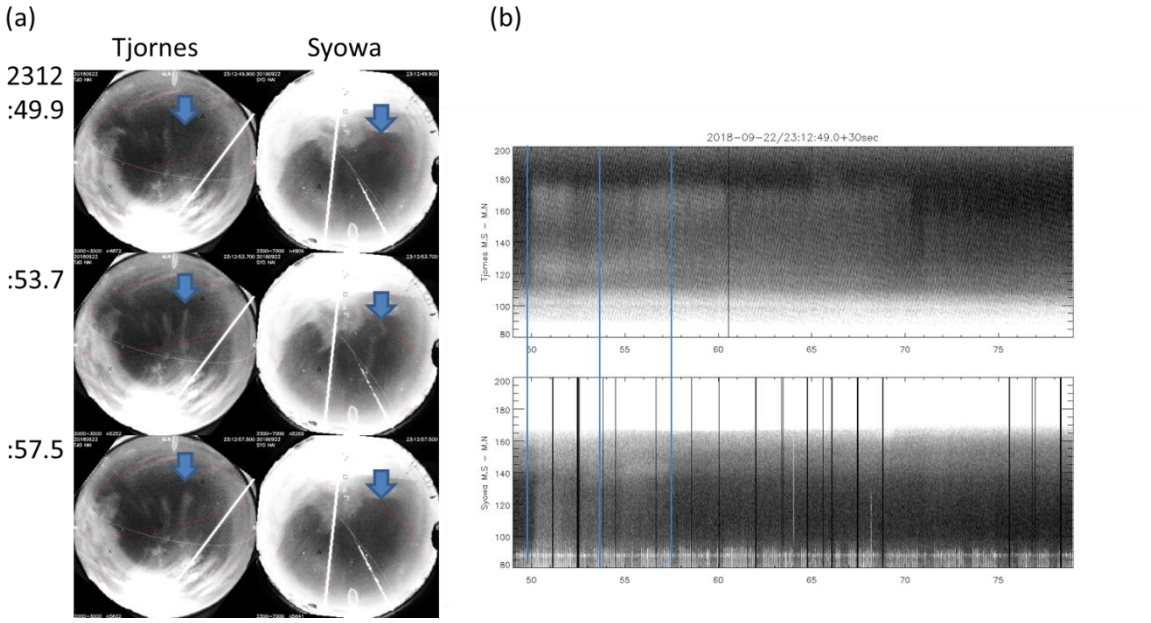

Figure 6-1: Example of isolated auroral patches observed by HAIs. (a) All-sky images of TJO and SYO captured at intervals of about 4 s beginning at 23:12:49.9 UT. (b) Keogram of the TJO and SYO patches cut in the magnetic N–S direction.

Second, it is apparent that the large shift of conjugate points cannot be fully investigated by the limited FOVs of the single conjugate pair of all-sky HAI. The existing data from other imagers, such as those located at Husafell in Iceland, and in Maitri and Princess Elisabeth Antarctica (PEA) in Antarctica, can extend the FOV in the local time direction and can therefore be useful to observationally elucidate the large shift in conjugate auroral phenomena in greater detail. For example, it is important to examine the development of the westward (eastward) side of the poleward expansion in the Northern (Southern) Hemisphere in the case of September 22, 2018, event. The Hall-current hypothesis predicts that the westward side did not evolve toward the west in the Northern Hemisphere as it did in the Southern Hemisphere. Many other substorm events

can also be used to test the hypothesis from this perspective even if the conjugate data are not available.

The data sets of the HAI itself are therefore useful for further detailed studies in the future. Efforts to make the data open and available to the public is still undergoing. At least basic calibration such as flat correction must be performed before resealing the data open to public. Thus far, only the quick-look daily keogram data of HAI are open to the public. The next step is to prepare the keogram data in Common Data Format (CDF) to be readily loaded by the Space Physics Environment Data Analysis System (SPEDAS) software, which is a common platform used in our field. SPEDAS facilitates the combination of data with many other data sets. Making HAI data easily obtained from the common SPEDAS platform will not only accelerate the research but might also lead to the discovery of facts that have been difficult to be noticed in the past. Further, we plan to convert all of the several tens of TB data of the 0.1 s integrated images to CDF format, which would be a total of a few tens of TB data.

Finally, future research must include further developments of the imaging system, particularly the creation of a maintenance-free system to extend the observation periods to decades or multiple solar cycles. Using Windows OS instead of Linux at the observation site makes remote operation easier and enables local collaborators to change the settings in the event of a problem. However, it will be necessary to introduce a somewhat simpler method of operation, such as one that automatically restarts the entire observation system after rebooting. Currently, large amounts of data are stored on HDDs that are exchanged every year. In the near future, however, it will be possible to transfer the observed data via network operation. Many other items exist for improving automatic observations. For example, the fixed time resolution at 100 fps is a problem in campaign

observations. A more flexible setting to easily conduct burst-mode observation would be helpful.

7. Concluding remarks

1. The purpose of this thesis was to observationally constrain the physical mechanism connecting the magnetosphere and the ionosphere by analyzing the poleward expansion and pulsating aurora based on ground-based high-speed observation. Targeting these two major themes of the aurora, this study began with the development of the necessary observation equipment. The developed HAI was installed at SYO and TJO in 2018. The system worked at a 100 fps sampling rate for the overwinter period almost continuously. Quick-look data can also be checked in daily bases via the website. For every season, ~100 TB of data were obtained at each site.

2. We reported the best example of the asymmetric spatiotemporal development of the propagating auroral structures that were observed by identical ground-based all-sky imagers at the N–S magnetic conjugate points. The large displacement of the conjugate points (1.7–2.3 MLT from the nominal conjugate points) were consistent with the theoretical expectations. The asymmetric propagating auroras were consistent with the expectations of the results from recent global MHD simulations, which supports the hypothesis that the direction of the Hall current plays an important role in controlling the development of substorm surges. The discrepancy between the position of the bright aurora and the position of the shear motion in the propagating aurora is an open question. A simulation with higher spatial resolution may reproduce the observed results in the future.

3. Rapid pulsating aurora were found to be caused also by chorus waves. Encouraging results were obtained to promote an understanding of wave–particle interaction in the highest-frequency domain at ~20 Hz.

8. References

Akasofu, S.-I. (1963). The dynamical morphology of the aurora polaris. Journal of Geophysical Research, 68(6), 1667 - 1673. https://doi.org/10.1029/JZ068i006p01667

Akasofu, S.-I. (1964). The development of the auroral substorm. Planetary and Space Science, 12(4), 273‐282. https://doi.org/10.1016/00320633(64)90151-5

Angelopoulos, V., Cruce, P., Drozdov, A., Grimes, E. W., Hatzigeorgiu, N., King, D. A., et al. (2019). The Space Physics Environment Data Analysis System (SPEDAS). Space Science Reviews, 215(1), https://doi.org/10.1007/s11214-018-0576-4

Baker, K. B., & Wing, S. (1989). A new magnetic coordinate system for conjugate studies at high latitudes. Journal of Geophysical Research, 94(a7), 9139. https://doi.org/10.1029/JA094iA07p09139

Carbary, J. F., Liou, K., Lui, A. T. Y., Newell, P. T., & Meng, C. ‐ I. (2000). “Blob” analysis of auroral substorm dynamics. Journal of Geophysical Research, 105(A7), 16,083–16,091. https://doi.org/10.1029/1999JA000210

Chaston, C. C., and K. Seki (2010), Small-scale auroral current sheet structuring, J. Geophys. Res., 115, A11221, doi:10.1029/2010JA015536.

Chaston, C. C. (2015) Inverted-V Auroral Arcs and Alfvén Waves, in Auroral Dynamics and Space Weather (eds Y. Zhang and L. J. Paxton), John Wiley & Sons, Inc, Hoboken, NJ. doi: 10.1002/9781118978719.ch3

Cowley, S. W. H. (1981). Magnetospheric asymmetries associated with the y ‐

component of the IMF. Planetary and Space Science, 29(1), 79–96. https://doi.org/10.1016/0032-0633(81)90141-0

Craven, J. D., & Frank, L. A. (1985). The temporal evolution of a small auroral substorm as viewed from high altitudes with Dynamics Explorer 1. Geophysical Research Letters, 12(7), 465–468. https://doi.org/10.1029/GL012i007p00465

DeWitt, R. N. (1962). The occurrence of aurora in geomagnetically conjugate areas. Journal of Geophysical Research, 67(4), 1347–1352. https://doi.org/10.1029/JZ067i004p01347

Ebihara, Y., & Tanaka, T. (2015a). Substorm simulation: Insight into the mechanisms of initial brightening. Journal of Geophysical Research: Space Physics, 120, 7270–7288. https://doi.org/10.1002/2015JA021516

Ebihara, Y., & Tanaka, T. (2015b). Substorm simulation: Formation of westward traveling surge. Journal of Geophysical Research: Space Physics, 120, 10,466–10,484. https://doi.org/10.1002/2015JA021697

Ebihara, Y., & Tanaka, T. (2018). Why does substorm‐associated auroral surge travel westward? Plasma Physics and Controlled Fusion, 60(1), 014024. https://doi.org/10.1088/1361-6587/aa89fd

Frank, L. A., Craven, J. D., Burch, J. L., & Winningham, J. D. (1982). Polar views of the Earth's aurora with Dynamics Explorer. Geophysical Research Letters, 9(9), 1001–1004. https://doi.org/10.1029/GL009i009p01001

Fukushima, N (1976). Generalized theorem for no ground magnetic effect of vertical currents connected with Pedersen currents in the uniform-conductivity ionosphere. Report of ionosphere and space research in Japan, Ionosphere Research

Committee, Science Council of Japan, Vol. 30, Nos. 1/2, pp. 35-40.

Gjerloev, J. W. (2012). The SuperMAG data processing technique. Journal of Geophysical Research, 117, A09213. https://doi.org/10.1029/2012JA017683

Haaland, S. E., Paschmann, G., Förster, M., Quinn, J. M., Torbert, R. B., McIlwain, C. E., et al. (2007). High‐latitude plasma convection from Cluster EDI measurements: Method and IMF‐dependence. Annales de Geophysique, 25(1), 239‐253. https://doi.org/10.5194/angeo-25-239-2007

Hosokawa, K., Miyoshi, Y., Ozaki, M. et al. Multiple time-scale beats in aurora: precise orchestration via magnetospheric chorus waves. Sci Rep 10, 3380 (2020). https://doi.org/10.1038/s41598-020-59642-8

Ieda, A., Kauristie, K., Nishimura, Y., Miyashita, Y., Frey, H. U., Juusola, L., et al. (2018). Simultaneous observation of auroral substorm onset in Polar satellite global images and ground-based all-sky images. Earth, Planets and Space, 70(1), 73. https://doi.org/10.1186/s40623-018-0843-3

Kadokura, A., A.-S. Yukimatu, M. Ejiri, T. Oguti, M. Pinnock, and M. R. Hairston (2002). Detailed analysis of a substorm event on 6 and 7 June 1989, 1, Growth phase evolution of nightside auroral activities and ionosheric convection toward expansion phase onset, J. Geophys. Res., 107(A12), 1479, doi:10.1029/2001JA009127

Kadokura, A., H. Yamagishi, S. Natsuo, K. Nakano, M. C. Rose (2008). Unmanned magnetometer network observation in the 44th Japanese Antarctic Research Expedition: Initial results and an event study on auroral substorm evolution. Polar Science, Volume 2, Issue 3, Pages 223-235,

https://doi.org/10.1016/j.polar.2008.04.002

Kan, J. R., & Kamide, Y. (1985). Electrodynamics of the westward traveling surge. Journal of Geophysical Research, 90(A8), 7615–7619. https://doi.org/10.1029/JA090iA08p07615

Kasahara, S., Y. Miyoshi, S. Yokota, T. Mitani, Y. Kasahara, S. Matsuda, A. Kumamoto, A. Matsuoka, Y. Kazama, H.U. Frey, V. Anvelopoulos, S. Kurita, K. Keika, K. Seki, and I. Shinohara (2018). Pulsating aurora from electron scattering by chorus waves, Nature, 554, 337-340, https://doi.org/10.1038/nature25505.

Kataoka, R., Y. Miyoshi, D. Hampton, T. Ishii, and H. Kozako (2012), Pulsating aurora beyond the ultra-low frequency range, J. Geophys. Res., 117, A08336, doi:10.1029/2012JA017987.

Kataoka, R., T. Nishiyama, Y. -M. Tanaka, A. Kadokura, H. A. Uchida, Y. Ebihara, M. K. Ejiri, Y. Tomikawa, M. Tsutsumi, K. Sato, Y. Miyoshi, K. Shiokawa, S. Kurita, Y. Kasahara, M. Ozaki, K. Hosokawa, S. Matsuda, I. Shinohara, T. Takashima, and T. Sato (2019), Transient ionization of the mesosphere during auroral breakup: Arase satellite and ground-based conjugate observations at Syowa Station, Earth, Planet and Space, 71, 9, https://doi.org/10.1186/s40623-019-0989-7.

Liou, K., Meng, C.-I., Lui, A. T. Y., Newell, P. T., & Wing, S. (2002). Magnetic dipolarization with substorm expansion onset. Journal of Geophysical Research, 107(A7), 1131. https://doi.org/10.1029/2001JA000179

Liou, K., Meng, C. I., & Wu, C. C. (2006). On the interplanetary magnetic field By control of substorm bulge expansion. Journal of Geophysical Research, 111, A09312. https://doi.org/10.1029/2005JA011556

Liou, K., & Mitchell, E. (2019). Effects of the interplanetary magnetic field y component on the dayside aurora. Geoscience Letter, 6(1), 1. https://doi.org/10.1186/s40562-019-0141-3

Liou, K., & Newell, P. T. (2010). On the azimuthal location of auroral breakup: Hemispheric asymmetry. Geophysical Research Letters, 37, L23103. https://doi.org/10.1029/2010GL045537

Liou, K., & Ruohoniemi, J. M. (2006). A case study of relationship between substorm expansion and global plasma convection. Geophysical Research Letters, 33, L02105. https://doi.org/10.1029/2005GL024736

Matsuoka, A., Teramoto, M., Nomura, R., Nose, M., Fujimoto, A., Tanaka, Y., et al. (2018). The ARASE (ERG) magnetic field investigation. Earth, Planets and Space, 70(1), 43. https://doi.org/10.1186/s40623-018-0800-1

Miyoshi, Y., Y. Katoh, T. Nishiyama, T. Sakanoi, K. Asamura, and M. Hirahara (2010). Time of flight analysis of pulsating aurora electrons, considering wave‐particle interactions with propagating whistler mode waves, J. Geophys. Res., 115, A10312, doi:10.1029/2009JA015127.

Miyoshi, Y., S. Oyama, S. Saito, S. Kurita, H. Fujiwara, R. Kataoka, Y. Ebihar, C. Kletzing, G. Reeves, O. Santolik, M. Clilverd, C. J. Rodger, E. Turunen, and F. Tsuchiya (2015). Energetic electron precipitation associated with pulsating aurora: EISCAT and Van Allen Probe observations, J. Geophys. Res., 120, Issue 4, Pages 2754-2766, doi: https://doi.org/10.1002/2014JA020690.

Miyoshi, Y., Hori, T., Shoji, M., Teramoto, M., Chang, T. F., Segawa, T., et al. (2018). The ERG science center. Earth, Planets and Space, 70(1), 96.

https://doi.org/10.1186/s40623-018-0867-8

Miyoshi, Y., Shinohara, I., Takashima, T., Asamura, K., Higashio, N., Mitani, T., et al. (2018). Geospace exploration project ERG. Earth, Planets and Space, 70(1), 101. https://doi.org/10.1186/s40623-018-0862-0

Morioka, A., Miyoshi, Y., Tsuchiya, F., Misawa, H., Kasaba, Y., Asozu, T., et al. (2011). On the simultaneity of substorm onset between two hemispheres. Journal of Geophysical Research, 116, A04211. https://doi.org/10.1029/2010JA016174

Motoba, T., Hosokawa, K., Sato, N., Kadokura, A., & Bjornsson, G. (2010). Varying interplanetary magnetic field By effects on interhemispheric conjugate auroral features during a weak substorm. Journal of Geophysical Research, 115, A09210. https://doi.org/10.1029/2010JA015369

Motoba, T., Hosokawa, K., Ogawa, Y., Sato, N., Kadokura, A., Buchert, S. C., & Rème, H. (2011). In situ evidence for interplanetary magnetic field induced tail twisting associated with relative displacement of conjugate auroral features. Journal of Geophysical Research, 116, A04209. https://doi.org/10.1029/2010JA016206

Nakamura, R., Oguti, T., Yamamoto, T., & Kokubun, S. (1993). Equatorward and poleward expansion of the auroras during auroral substorms. Journal of Geophysical Research, 98(A4), 5743–5759. https://doi.org/10.1029/92JA02230

Nishimura, Y., J. Bortnik, W. Li, R. M. Thorne, L. R. Lyons, V. Angelopoulos, S. B. Mende, J. W. Bonnell, O. Le Contel, C. Cully, R. Ergun and U. Auster (2010). Identifying the drive of pulsating aurora, Science, 330, 81–84, https://doi.org/10.1126/science.1193186.

Nishimura, Y., J. Bortnik, W. Li, R. M. Thorne, L. Chen, L. R. Lyons, V. Angelopoulos,

S. B. Mende, J. Bonnell, O. Le Contel, C. Cully, R. Ergun and U. Auster (2011). Multievent study of the correlation between pulsating aurora and whistler mode chorus emissions, Journal of Geophysical Research, 116, A11221, https://doi.org/10.1029/2011JA016876.

Nishimura, Y., M. R. Lessard, Y. Kato, Y. Miyoshi, E. Grono, N. Partamies, N. Sivadas, K. Hosokawa, M. Fukizawa, M. Samara, R. G. Michell, R. Kataoka, T. Sakanoi, and D. K. Whiter (2020). Diffuse and Pulsating Aurora, Space Science Reviews, Space Sci Rev, 216, 4. https://doi.org/10.1007/s11214-019-0629-3.

Ohma, A., Østgaard, N., Reistad, J. P., Tenfjord, P., Laundal, K. M., Snekvik, K., et al. (2018). Evolution of asymmetrically displaced footpoints during substorms. Journal of Geophysical Research: Space Physics, 123, 10,030–10,063. https://doi.org/10.1029/2018JA025869

Østgaard, N., Mende, S. B., Frey, H. U., Immel, T. J., Frank, L. A., Sigwarth, J. B., & Stubbs, T. J. (2004). Interplanetary magnetic field control of the location of substorm onset and auroral features in the conjugate hemispheres. Journal of Geophysical Research, 109, A07204. https://doi.org/10.1029/2003JA010370

Østgaard, Nikolai, Reistad, Jone P., Tenfjord, Paul, Laundal, Karl M., Rexer, Theresa, Haaland, Stein E., et al. (2018). The asymmetric geospace as displayed during the geomagnetic storm on 17 August 2001. Annales Geophysicae, 36(6), 1577–1596. https://doi.org/10.5194/angeo-36-1577-2018

Østgaard, N., Tsyganenko, N. A., Mende, S. B., Frey, H. U., Immel, T. J., Fillingim, M., et al. (2005). Observations and model predictions of substorm auroral asymmetries in the conjugate hemispheres. Geophysical Research Letters, 32,

L05111. https://doi.org/10.1029/2004GL022166

Ozaki, M., et al. (2018). Microscopic observations of pulsating aurora associated with chorus element structures: Coordinated Arase satellite-PWING observations, Geophys. Res. Lett., 45, 12,125-12,134, https://doi.org/10.1029/2018GL079812.

Ozaki M., et al. (2019). Visualization of rapid electron precipitation via chorus element wave-particle interactions, Nature Comm., 10, 257.

Rothwell, P. L., Silevitch, M. B., & Block, L. P. (1984). A model for the propagation of the westward traveling surge. Journal of Geophysical Research, 89(A10), 8941. https://doi.org/10.1029/JA089iA10p08941

Royrvik, O., and T. N. Davis (1977). Pulsating aurora: Local and global morphology, Journal of Geophysical Research, 82, 4720–4740, https://doi.org/10.1029/JA082i029p04720.

Saita, S., Kadokura, A., Sato, N., Fujita, S., Tanaka, T., Ebihara, Y., et al. (2011). Displacement of conjugate points during a substorm in a global magnetohydrodynamic simulation. Journal of Geophysical Research, 116, A06213. https://doi.org/10.1029/2010JA016155.

Sandahl, I., L. Eliasson, and R. Lundin (1980). Rocket observations of precipitating electrons over a pulsating aurora, Geophysical Research Letters, 7, 309–312, https://doi.org/10.1029/GL007i005p00309.

Santolik, O., D. A. Gurnett, and J. S. Pickett (2004). A microscopic and nanoscopic view of storm-time chorus on 31 March 2001, Geophysical Research Letters, 31, L02801, doi:10.1029/2003GL018757

Santolík, O., C. A. Kletzing, W. S. Kurth, G. B.Hospodarsky, and S. R. Bounds (2014), Finestructure of large-amplitude chorus wavepackets, Geophysical Research Letters, 41,293–299, doi:10.1002/2013GL058889.

Sato, N., Nagaoka, T., Hashimoto, K., & Saemundsson, T. (1998). Conjugacy of isolated auroral arcs and nonconjugate auroral breakups. Journal of Geophysical Research, 103(A6), 11,641–11,652. https://doi.org/10.1029/98JA00461.

Sato, N., & Saemundsson, T. (1987). Conjugacy of electron auroras observed by all-sky cameras and scanning photometers. Memoirs of National Institute of Polar Research. Special Issue, 48, 58–71.

Shepherd, S. G. (2014). Altitude‐adjusted corrected geomagnetic coordinates: Definition and functional approximations. Journal of Geophysical Research: Space Physics, 119, 7501–7521. https://doi.org/10.1002/2014JA020264

Stenbaek-Nielsen, H. C., Davis, T. N., & Glass, N. W. (1972). Relative motion of auroral conjugate points during substorms. Journal of Geophysical Research, 77(10), 1844–1858. https://doi.org/10.1029/JA077i010p01844

Stenbaek‐Nielsen, H. C., & Otto, A. (1997). Conjugate auroras and the interplanetary magnetic field. Journal of Geophysical Research, 102(A2), 2223–2232. https://doi.org/10.1029/96JA03563

Tanaka, T. (2015). Substorm Auroral Dynamics Reproduced by Advanced Global Magnetosphere-Ionosphere (M-I) Coupling Simulation, Auroral Dynamics and Space Weather. Hoboken, NJ: John Wiley & Sons, Inc, pp. 177–190. doi:10.1002/9781118978719.ch13.

Tanaka, Y., Ogawa, Y., Kadokura, A., Partamies, N., Whiter, D., Enell, C. F., et al. (2015).

Eastward-expanding auroral surges observed in the post‐midnight sector during a multiple‐onset substorm. Earth, Planets and Space, 67(1), 182. https://doi.org/10.1186/s40623-015-0350-8

Tanaka, T., Y. Ebihara, K. Watanabe, M. Den, S. Fujita, T. Kikuchi, K. Hashimoto, and R. Kataoka (2019a). Development of magnetic topology during the growth phase of the substorm inducing the onset of the near-Earth neutral line. Journal of Geophysical Research: Space Physics, 124, 5158-5183. https://doi.org/10.1029/2018JA026386.

Tanaka, T., Y. Ebihara, K. Watanabe, M. Den, S. Fujita, T. Kikuchi, K. Hashimoto, and R. Kataoka (2019b). Why the initial brightening starts from the equatorward-most growth phase arc?, submitted to JGR Space Physics, 2019JA027157.

Tanaka, Y.-M., Nishiyama, T., Kadokura, A., Ozaki, M., Miyoshi, Y., Shiokawa, K., et al. (2019). Direct Comparison Between Magnetospheric Plasma Waves and Polar Mesosphere Winter Echoes in Both Hemispheres. Journal of Geophysical Research: Space Physics, 124(11), 9626–9639. https://doi.org/10.1029/2019JA026891

Tsyganenko, N. A., & Sitnov, M. I. (2005). Modeling the dynamics of the inner magnetosphere during strong geomagnetic storms. Journal of Geophysical Research, 110, A03208. https://doi.org/10.1029/2004JA010798

Uchida, H. A., R. Kataoka, A. Kadokura, K. Murase, A. S. Yukimatu, Y. Miyoshi, K. Shiokawa, Y. Ebihara, K. Hosokawa, A. Matsuoka, S. Kurita, S. Fujita, I. Shinohara (2020). Asymmetric development of auroral surges in northern and southern hemispheres, Geophysical Research Letters, 47, e2020GL088750.

https://doi.org/10.1029/2020GL088750.

Wescott, E. M. (1966). Magnetoconjugate phenomena. Space Science Reviews, 5(4), 507–561. https://doi.org/10.1007/BF00240576

Yamamoto, T. (1988). On the temporal fluctuations of pulsating auroral luminosity, Journal of Geophysical Research, 93, 897–911, doi:10.1029/JA093iA02p00897.